Edinburgh Research Explorer

An experimental investigation of F, Cl and H2O mineral-melt partitioning in a reduced, model lunar system

OPEN ACCESS

1 **An experimental investigation of F, Cl and H_2O mineral-melt partitioning in a reduced,**
2 **model lunar system.**
3

4 Nicola J. Potts[1], Geoffrey D. Bromiley[1,2*], Richard A. Brooker[3]
5

6 [1]School of GeoSciences, Grant Institute, University of Edinburgh, Edinburgh, UK.
7 [2]Centre for Science at Extreme Conditions, University of Edinburgh, UK.
8 [3]School of Earth Sciences, University of Bristol, Bristol, UK
9

10 *corresponding author: geoffrey.bromiley@ed.ac.uk
11
12

13 **Abstract**
14

15 It is believed that the Moon formed following collision of a large planetesimal with the early
16 Earth. Over the ~4 Gyr since this event the Moon has been considerably less processed by
17 geological activity than the Earth, and may provide a better record of processes and conditions
18 in the early Earth-Moon system. There have been many studies of magmatic volatiles such as
19 H, F, Cl, S and C in lunar materials. However, our ability to interpret variable volatile contents
20 in the lunar sample suite is dependent on our understanding of volatile behaviour in lunar
21 systems. This is currently constrained by limited experimental data. Here, we present the first
22 experimental mineral-melt partitioning coefficients for F, Cl and H_2O in a model lunar system
23 under appropriately reduced conditions (log fO_2 to IW-2.1, i.e. oxygen fugacity down to 2.1 log
24 units below the Fe-FeO buffer). Data are consistent with structural incorporation of F, Cl and
25 OH^- in silicate melt, olivine and pyroxene under conditions of the lunar mantle. Oxygen fugacity
26 has a limited effect on H_2O speciation, and partitioning of H_2O, F and Cl is instead largely
27 dependent on mineral chemistry and melt structure. Partition coefficients are broadly
28 consistent with a mantle source region for lunar volcanic products that is significantly depleted
29 in F, Cl and H_2O, and depleted in Cl relative to F and H_2O, compared to the terrestrial mantle.
30 Partitioning data are also used to model volatile redistribution during lunar magma ocean
31 (LMO) crystallisation. The volatile content of lunar mantle cumulates is dependent upon
32 proportion of trapped liquid during LMO solidification. However, differences in mineral-melt
33 partitioning during LMO solidification can result in significant enrichment on F relative to Cl,
34 and F relative to H_2O, in cumulate phases relative to original LMO composition. As such, Cl
35 depletion in lunar volcanic products may in part be a result of LMO solidification.
36
37

38 **1. Introduction**
39

40 The presence of 'water' or related H-bearing species, i.e. H_2O, OH^-, H_2 etc, in the interior of
41 the Earth has a controlling influence on a range of mantle properties from melting behaviour
42 to rheology (Peslier, 2010, and references therein). The additional role of water in sustaining
43 life means that the origin of Earth's volatiles and the timing of their delivery are key areas of
44 study in Earth and planetary sciences. However, many geological processes have modified
45 the Earth since its initial formation, redistributing these volatiles and masking geochemical
46 signatures of their origin. If it is accepted that the Earth and Moon share some common history,
47 the question is when did their compositions diverge and to what extent (Albarède, 2009).
48 According to the canonical "Giant Impact" hypothesis, the Moon formed following collision of

49   a Mars-sized planetesimal with the early Earth (Canup and Agnor, 2000; Canup, 2004). This
50   catastrophic heating event was previously believed to be consistent with an anhydrous lunar
51   interior and lunar sample suite (Lucey et al., 2006; Taylor et al., 2006). The subsequent
52   detection of water and other volatiles in volcanic lunar glasses (Saal et al., 2008) has heralded
53   a new era of lunar research and reinvestigation of the lunar sample suite. This has revealed
54   the presence of 'water' in volcanic lunar glasses (Saal et al., 2008, 2013; Greenwood, 2018),
55   in apatites in mare basalts (Boyce et al., 2010; McCubbin et al., 2010a; McCubbin et al.,
56   2010b; Greenwood et al., 2011; Barnes et al., 2013; Greenwood, 2018), in olivine-hosted melt
57   inclusions in mare basalts (Chen et al., 2015; Hauri et al., 2011; Hauri et al., 2015; Ni et al.,
58   2017; Ni et al., 2019), in plagioclase from lunar anorthosites (Hui et al., 2013; 2017), as well
59   as halogens in mesostasis in lunar basalts (Greenwood et al., 2020). It is now clear that
60   various lunar mantle source regions contain appreciable H, in addition to Cl, F, C and S. As
61   the Moon shares a common origin with the Earth, the logical conclusion is that a similar
62   process may have been involved in volatile delivery to both components of the early Earth-
63   Moon system. Volatiles were either delivered to the Earth prior to the Moon-forming event or
64   delivered to the Earth-Moon system shortly after the Moon-forming event, whilst the newly-
65   formed Moon was still in a largely molten state. As the Moon has remained less affected by
66   large-scale geological processes since its formation, the lunar volatile budget may provide
67   much needed insight into the early Earth-Moon system, and ultimately, provide constraints on
68   the origin of Earth's hydrosphere.
69
70   The lunar sample suite is consistent with a high temperature origin for the Moon. For example,
71   the lunar anorthositic crust probably represents a plagioclase floatation crust formed during
72   lunar magma ocean (LMO) solidification (Warren, 1985). The later mare basalts most likely
73   formed by partial melting of deeper mantle cumulates, also produced by the same LMO
74   solidification process, following late-stage cumulate overturn (Ryder, 1991). As a result, the
75   volatile content of mare basalts and associated volcanic glasses provides insight into the
76   volatile budget of the lunar mantle melts and the LMO solidification products (e.g. Hauri et al.
77   2011; Saal et al. 2008). With the detection of 'water' in lunar materials and inferred 'water'
78   contents in parental lunar magmas, it is tempting to make direct comparison with terrestrial
79   magmas. For example, Hauri et al. (2011) noted that volatile contents of melt inclusions in
80   lunar olivine are similar to those in terrestrial mid-ocean ridge basalts, implying similar volatile
81   budgets in terrestrial and lunar mantle source regions. However, any such comparison can be
82   misleading because of differences in magmatic conditions between evolved terrestrial and
83   lunar systems. Mare basalts and associated volcanic glasses are reduced compared to
84   terrestrial volcanic materials, with mineral assemblages and direct oxygen fugacity (fO_2)
85   measurements indicating fO_2 below that of the iron-wüstite (IW, i.e. Fe-FeO) solid buffer, and
86   either at or near Fe-metal saturation (Longhi, 1992; Shearer et al., 2006). The reduced nature
87   of lunar magmas implies melting of a similarly reduced lunar interior (Longhi, 1992), with the
88   oxidation state of the source region for mare basalts and volcanic glasses generally assumed
89   to be at least 2 log units lower than Earth's upper mantle (Rutherford and Papale, 2009; Sato,
90   1976). Oxygen fugacity has a fundamental control on 'water' or H incorporation in silicate
91   materials. In terrestrial systems at high mantle temperatures and pressures 'water' is
92   incorporated into nominally anhydrous minerals such as olivine and pyroxenes as interstitial
93   H associated with underbonded O atom sites (e.g. Skogby et al., 1990; Smyth et al., 1991;
94   Ingrin and Skogby, 2000; Stalder and Skogby, 2003; Bromiley et al., 2004; Bromiley and
95   Bromiley, 2006; Smyth et al., 2006), forming various O-H defects (Lemaire et al., 2004;
96   Matveev et al, 2005; Grant et al, 2007). In terrestrial silicate melts, water is incorporated initially

97   as OH⁻, with molecular H_2O becoming more dominant at higher total water contents, at least
98   under more oxidising conditions (e.g. Stolper, 1982; Pandya et al., 1992; Dixon et al., 1995).
99   This has recently been contested by Cody et al. (2020) who suggest that H_2O dominates at
100   low H abundances, at least in highly polymerised silicate melts, although whether this is true
101   in less polymerised, basaltic melts remains unclear. Under reducing conditions H_2O becomes
102   unstable as a species, and other H-related defects such as H_2 and CH_4 are observed in
103   spectroscopic investigations of melts at the expense of OH⁻ (Kadik et al., 2006; Mysen et al.,
104   2011; Hirschmann et al., 2012; Ardia et al., 2013). Magmas are commonly used as probes of
105   planetary interiors as they represent escaped partial melts that transport information about
106   source regions. The 'water' content of magmas is controlled in part by mineral-melt partitioning
107   during partial melting of the mantle source. Any change in speciation of 'water' as a function
108   of fO_2 could result in significant changes in partitioning. The 'water' content of a magma will
109   likely depend on both the H concentration and the fO_2 in its mantle source region, and any
110   comparison between lunar and terrestrial magmas must take this into account. Kadik et al.
111   (2006) noted that at high pressure in silicate melts at fO_2 below IW, H_2 becomes increasingly
112   important at the expense of more oxidised species. Hirschmann et al. (2012) noted that the
113   proportion of H_2 in lunar magmas is low under the low total water contents of the lunar interior.
114   However, in reduced lunar systems over a range of inferred bulk 'water' contents (Elkins-
115   Tanton and Grove, 2011) the proportion of H_2/H_2+H_2O could range up to 20-50%. In solid
116   phases under similarly reducing conditions, Yang et al. (2016) demonstrated that mantle
117   silicates can also incorporate some molecular H_2, in addition to OH defects. The effects of any
118   change in speciation on volatile behaviour remain unclear. Newcombe et al. (2017)
119   demonstrated that degassing mechanisms in lunar melts over a range of highly reducing
120   conditions (below the IW buffer) are strongly controlled by H speciation, although they noted
121   that diffusion is dominated by flux of OH⁻ rather than H_2. Recently, Lin et al. (2019)
122   demonstrated that fO_2 has a strong control on H_2O partitioning between plagioclase and
123   silicate melt, but aside from that study there is an absence of data on the effect of fO_2 on
124   volatile partitioning in lunar systems. Here we present the first experimental data on
125   partitioning of H_2O, F and Cl in a reduced, model lunar mantle lithology system. F and Cl are
126   important tracers in lunar materials (e.g. Hauri et al., 2011; Chen et al., 2015), and are
127   increasingly used to provide insight into volatile redistribution during terrestrial geological
128   processes (e.g. Urann et al., 2017; Klemme and Stalder, 2018). Furthermore, isotopic
129   variations of Cl in lunar materials provide significant additional insight into lunar magmatic
130   processes (McCubbin et al., 2011; Potts et al., 2018; Boyce et al., 2018). Therefore, combined
131   study of F, Cl and H_2O distribution during magmatic processes provides a powerful tool for
132   reinvestigating the importance of measured volatile concentrations in lunar samples, and for
133   drawing inferences on volatile delivery to the early Earth-Moon system.
134
135
136 **2. Methods**
137 **2.1   System and bulk composition**
138
139   To constrain volatile mineral-melt partitioning during lunar mantle melting, a synthetic starting
140   material was used with a composition similar to lunar low-Ti, picritic, green volcanic glass
141   beads. These pyroclastic glasses are believed to be amongst the most primitive lunar samples
142   (Delano, 1979) and suggested to represent partial melts from lunar mantle cumulates formed
143   at around 1.5 to 2.5 GPa (Shearer et al., 2006). A composition, corresponding to an average
144   green lunar glass from Saal et al. (2008) was chosen (Table 1). This composition is close to

145 that of Apollo 15A green glasses that best represent primitive lunar melts with minimal mantle
146 cumulate assimilation (Barr and Grove, 2007).

147

148 A homogenous, reduced starting material was made by first grinding high-purity oxides (SiO_2,
149 Al_2O_3, MgO, TiO_2, Fe_2O_3, Cr_2O_3) and carbonates (Na_2O, $CaCO_3$, K_2CO_3), under isopropanol
150 in an agate pestle and mortar for 40 minutes. Prior to weighing, SiO_2, TiO_2, MgO, and Al_2O_3
151 were fired at 1000 °C in a box furnace for 24 hours. These were then stored in a 110 °C oven
152 with the other powders. After grinding, the mixture was transferred to an Fe-saturated Pt
153 crucible and decarbonated in a box furnace from 600 to 900 °C over eight hours. The mixture
154 was removed from the furnace and stored in a 110 °C oven while the furnace was raised to
155 1550 °C. The mixture was then inserted into the hot spot of the furnace for 30 minutes. The
156 mixture was removed and quenched to a homogenous glass by inserting the bottom of the Pt
157 crucible in water, and then reground. The resulting fine powder was placed in an Fe-saturated
158 Pt crucible and reduced in a 1 atmosphere furnace at 1200 °C for 24 hours using a CO_2-H_2
159 gas mix equivalent to two log units below the iron-wustite buffer (IW-2; log $fO2$ = -14.6). After
160 regrinding, halogens and water were added as CaF_2 and $CaCl_2$ and $Al(OH)_3$. Al and Ca
161 proportions prior to glassing were calculated so that addition of volatiles resulted in the final,
162 desired bulk composition.

163

164

165 **2.2   High-pressure experiments**

166

167 Encapsulation techniques for highly reduced, high pressure experiments are challenging with
168 a high failure rate resulting from a loss of capsule integrity (physical or chemical; see section
169 3). After much trial and error, two capsule designs were used for these high-pressure volatile-
170 bearing experiments. To ensure that fO_2 remained below IW we developed a capsule
171 consisting of a 4 mm diameter high-purity (99.99%+) Fe metal outer capsule with hammer-fit
172 lid. This capsule acts as a sink for any excess O_2 present in the starting mix or introduced
173 during loading and also ensures that melts remain at/near Fe metal saturation. This use of
174 high-purity iron follows pioneering experiments on mare basalts (e.g. Longhi, 1992; Walker et
175 al., 1975). The starting mix was loaded into the capsule along with a welded 2mm diameter
176 inner Pt capsule containing a solid Cr-Cr_2O_3 buffer. During high pressure/temperature
177 experiments the reaction:

178

179     $2Cr + 1.5O_2 = Cr_2O_3$ [1]

180

181 within the Pt capsule buffers fO_2 at several log units below the IW buffer (Holzheid and O'Neill,
182 1995) at least while both Cr metal and Cr_2O_3 are present. In theory, H diffusion through the
183 thin (0.1 mm thick) Pt inner capsule allows fO_2 conditions within the inner capsule to be
184 transmitted to the outer capsule and sample, as in other double capsule techniques. However,
185 under reducing conditions Cr metal reacts with Pt to form a mixed Pt-Cr phase, implying
186 reaction [1] describes oxidation of the Cr component in a binary alloy, rather than an end-
187 member reaction. However, the success of this technique has been demonstrated by Stokes
188 et al. (2019) who used Fe XANES spectra to demonstrate that a Cr-based buffer can maintain
189 reducing conditions below IW, and this is further verified here by the presence of metallic iron
190 in run products, as described below. A second capsule design was used to purposely buffer
191 fO_2 closer IW and to allow direct comparison with previous studies. This design involved
192 loading the starting material into a graphite capsule with press fit lid which was then loaded

193 into a welded Pt outer capsule. The graphite bucket in this standard double capsule design
194 buffers fO_2 at C-CO, which in hydrous systems equates to roughly IW+2 to IW-1 depending
195 on run temperature, pressure and nature of sample (e.g. Armstrong et al., 2015).
196
197 Experiments were performed in an end-loaded piston cylinder apparatus. For Pt+graphite runs
198 (Pt_C), experiments were pressurised to ~0.5 GPa before simultaneously heating while
199 pressurising, until run values were reached. For Fe capsule runs (Fe), experiments were fully
200 pressurised before heating to ensure the capsules were closed (pressure welded). All runs
201 were heated at ~100°C/min, taken to the final run temperature and held for 24 hours. Rapid,
202 isobaric quenching was achieved by turning off power to the system whilst maintaining run
203 pressures. A fuller description of high-pressure experiments is given in Bromiley et al. (2017).
204 Experimental conditions were chosen to mimic near-liquidus experiments in lunar systems,
205 and synthesize mantle phases in equilibrium with high fraction silicate melt (e.g Longhi, 1992).
206
207
208 **2.3 Sample preparation and analysis**
209
210 Recovered capsules were sectioned using a 2 µm diamond wire saw. Both halves of capsules
211 were mounted in crystal bond, then ground and polished with diamond suspensions. Samples
212 were removed from crystal bond by dissolving in high-purity acetone, mounted in indium, and
213 C coated for visual inspection and analysis using a Scanning Electron microscope fitted with
214 quantitative Energy Dispersive Spectrometer (SEM-EDS). After SEM-EDS analysis, the C
215 coat was carefully removed from samples by buffing surfaces with a 0.25 µm diamond
216 suspension. At this stage one half of the capsule was removed from the indium mount, glued
217 onto a glass slide with crystal bond polished side down, and ground down to produce 300 µm
218 thick section. These were then removed from the glass slide with acetone and thoroughly
219 cleaned in ethanol for investigation by Fourier Transform Infrared (FTIR) spectroscopy.
220 However, due to the friable nature of run products only a limited number of experimental
221 charges could be successfully prepared in this way. Experiments run in graphite-lined platinum
222 capsules did not survive wafering. Instead, polished run products in mounts were analysed
223 using a Raman Imaging microscope to identify absorption due H-related species. For all
224 experiments, the remaining half of the capsule was gold coated and used for determination of
225 F, Cl, H and C contents by Secondary Ion Mass Spectrometry (SIMS) analysis.
226
227 F, Cl, H and C contents of samples were determined by secondary ion mass spectrometry
228 (SIMS) using a Cameca 4f instrument at The University of Edinburgh NERC Ion Microprobe
229 Facility. Prior to analysis, samples were kept in a vacuum oven for at least a week to reduce
230 H backgrounds. Samples were then gold coated before immediately being loading into the
231 relevant instruments vacuum chamber, and kept under vacuum (<5x10^{-8} mbar) for at least 48h
232 prior to analysis. A 5 nA negative ^{16}O ion beam accelerated to 10 kV was used for all
233 measurements. Secondary ions were accelerated to 4500 V minus a 75 eV energy offset for
234 F, Cl and H measurements, and 50 eV offset for C. Beam diameter was approximately 20 µm.
235 Each analysis area was pre-sputtered for 3 minutes with a 30 µm rastered beam, then spots
236 were analysed using a 10 µm small field aperture, avoiding any cracks, crystal edges and
237 inclusion within samples. Depth of analysis pits was <2 µm, and after SIMS analysis all
238 samples were imaged again using the SEM to ensure that analysis pits did not reveal presence
239 of any source of contamination. Each measurement consisted of 10 cycles, although the first
240 5 cycles for H_2O measurements were discounted to minimise surface contamination. CO_2 was

241 measured first with high mass resolution sufficient to resolve interference by $^{24}Mg^{2+}$ on the
242 $^{12}C^+$ peak. CO_2 and H_2O-bearing experimental basaltic glasses (ST) from Shishkina et al.
243 (2010) were used as primary standards for both CO_2 and H_2O, with anhydrous San Carlos
244 olivine standard additionally used to determine H_2O backgrounds, and NIST-SRM610, BCR-
245 2G and KL2-G used as secondary standards. Presence of volatile-bearing inclusions was
246 discounted by monitoring $^1H/^{30}Si$ signals. F and Cl concentrations were normalised to the ^{30}Si
247 count rate and calibrated using VG-2 (basaltic glass, Juan de Fuca ridge, #111240/52), VG-
248 A99 (basaltic glass, Makaopuhi lava lake, Hawaii, #113498/1), GSD-1G (basaltic glass,
249 USGS), and BIR-01G (basaltic glass) standards (Jochum et al., 2005). NIST-SRM610 and
250 BCR-2G glasses were used as a secondary standard and San Carlos olivine as a background
251 blank.
252
253 Electron probe microanalysis (EMPA) was used to determine mineral and melt major element
254 composition using a Cameca SX100 instrument running at 15 keV and the following
255 conditions/standards/analysing crystals: for glass, 2 nA and an 8 μm beam for Na (jadeite,
256 LTAP), Mg (spinel, LTAP), Al (spinel, LTAP), Fe (fayalite, LLIF), Ca (wollastonite, PET and
257 LPET), Si (wollastonite, TAP), and a 8 nA, 80 μm beam for Ti (rutile, PET and LPET), Cl (NaCl,
258 PET and LPET), F (SrF_2, TAP and LTAP), Cr (metal, LLIF) and Mn (metal, LLIF). For
259 orthopyroxene and olivine a 4 nA, 2μm beam was used for Fe (fayalite, LLIF), Mg (forsterite,
260 LTAP) and Si (forsterite, TAP), and a 100 nA, 2 μm beam for Ca (wollastonite, PET), Ti (rutile,
261 PET), Na (jadeite, LTAP), Cr (metal, LLIF) and Al (spinel, LTAP). For clinopyroxene analyses
262 a 4 nA, 2μm beam was used Mg (spinel, LTAP), Si (wollastonite, TAP), Al (spinel, LTAP), Fe
263 (fayalite, LLIF), Ca (wollastonite, PET), and a 100 nA, 2μm beam for Ti (rutile, PET), Na
264 (jadeite, LTAP) and Cr (metal, LLIF).
265
266 FTIR and Raman spectroscopy was used to provide information on H and C speciation and
267 bonding environment in recovered samples. Spectra were obtained from polished, sectioned
268 samples in transmission mode using a Thermo-Nicolet iN10MX IR microscope at the School
269 of Earth Sciences, University of Bristol. Samples were placed on thin BaF_2 plates, and
270 unpolarised spectra collected over the range 4000-450 cm^{-1} at a 4cm^{-1} spectral resolution,
271 using a variable shaped aperture to avoid cracks and inclusions within grains. Background
272 spectra were obtained through the BaF_2 plate prior to each transect, and automatically
273 subtracted from sample spectra. Raman spectra were obtained using a Thermo Scientific
274 DXRxi Raman Imaging microscope, also at the School of Earth Sciences, University of Bristol,
275 using a 532nm (green) doubled Nd:YVO$_4$ DPSS excitation laser, a 400 lines mm^{-1} extended
276 range grating, a 50x objective, a 25μm confocal pinhole and EMCCD detector. Approximately
277 1550 data points were acquired from 50-6000 cm^{-1}, typically at a laser power of 9 mW for
278 between 0.3 and 4s, averaged over 600-1000 scans.
279
280 **3. Results**
281 **3.1 Phase and melt relations in recovered samples.**
282
283 Most experiments were conducted at 2 GPa as this is an approximate pressure for multiple
284 mineral saturation in low-Ti picritic lunar systems, and within the range of estimates for the
285 pressure of formation of mare basalts and associated picritic glasses (Elkins-Tanton et al.,
286 2003; Shearer et al., 2006). Run products consisted of quenched glass with some minor
287 growth of quench crystals, and coexisting crystals of olivine, orthopyroxene, and pigeonite.
288 There was no evidence of a fluid phase in any experiment. This is consistent with the relatively

6

289   low amount of volatiles loaded (or derived from the graphite) which is below fluid saturation in
290   the melt for most of the expected species at these pressures. Experimental details and run
291   products are listed in Table 2, and SEM images representative of run products are shown in
292   Figure 1. High failure rate was noted in initial experiments, in part because the effect of low
293   fO_2 under H-rich conditions appears to stiffen and embrittle many metals, including Pt and Fe
294   capsules, which ensure the integrity of the experiment.
295

296   Run Fe_2 is an example of an earlier experimental design where sample charge and buffer
297   were separated by Pt foil. As evident in Figure 1A, melt from the experimental charge leaked
298   and partially reacted with the buffer during the experiment. Reaction resulted in Cr-enrichment
299   of the experimental charge and precipitation of a Cr-spinel phase not seen in other
300   experiments. The experimental charge also contains an Fe-rich metal phase, common with all
301   experiments conducted using Fe capsules, and attesting to Fe-saturated, reducing conditions.
302   In subsequent experiments the buffer mix was sealed within a welded Pt capsule (Figure 1B),
303   a design with a significantly higher success rate despite Pt embrittlement under run conditions.
304   However, glass compositions (Table 3) demonstrate that high run temperatures still result in
305   Cr gain in the silicate run products due to solid state diffusion and/or alloying of Cr with the Pt
306   capsule. Various experimental designs were trialed to circumvent this issue, including
307   alternative capsule materials and solid buffers. However, alloying remained an issue in all
308   designs, and other designs had higher failure rates. Therefore, we adopted the Fe-Pt-Cr-Cr_2O_3
309   design for the limited number of subsequent experiments described here.
310

311   Use of Fe capsules and reduced starting materials results in reducing, Fe-saturated run
312   conditions at or below IW. Run fO_2 is further buffered by reaction of Cr and Cr_2O_3, although
313   this is complicated by alloying of Cr with Pt. A lack of thermodynamic data on the Pt-Cr system
314   means that fO_2 cannot readily be calculated from the sample assembly. However, the
315   presence of a free Fe phase in run products using Fe capsules means that fO_2 can be
316   estimated based on the exchange of Fe between silicate melt and the Fe-phase:
317

318     $Fe_{metal}^0 + \tfrac{1}{2}O_2 = FeO_{melt}$ [2]
319

320   The equilibrium constant for [2] can be expressed as:
321

322     $\log K = \log(a_{FeO}^{melt}/a_{Fe}^{metal}) - \tfrac{1}{2}\log fO_2 = \log(X_{FeO}^{melt} \cdot \gamma_{FeO}^{melt} / X_{Fe}^{metal} \cdot \gamma_{Fe}^{metal}) - \tfrac{1}{2}\log fO_2$ [3]
323

324   where a_{FeO}^{melt} and a_{Fe}^{metal} are the activities of FeO in silicate melt and Fe in Fe metal,
325   respectively, where fO_2 is oxygen fugacity under experimental conditions, and X and γ
326   corresponding mole fractions and activity coefficients for each. For pure Fe metal and pure
327   FeO, i.e. the IW buffer, activities are unity and [3] can be expressed as:
328

329     $\log K = \tfrac{1}{2} \log fO_2^{IW}$ [4]
330

331   where fO_2^{IW} is the oxygen fugacity of the IW buffer under experimental conditions. Combining
332   (3) and (4):
333

334     $2 \log(X_{FeO}^{melt} \cdot \gamma_{FeO}^{melt} / X_{Fe}^{metal} \cdot \gamma_{Fe}^{metal}) = \Delta \log fO_2^{IW}$
335

336 demonstrates that concentrations of FeO in the melt phase, and Fe in the metal phase can be
337 used to determine fO_2 under run conditions relative to the IW buffer. Data from O'Neill and
338 Eggins (2002) was used to estimate γ_{FeO}^{melt}. Assuming that the Fe phase in experiments is
339 pure Fe implies fO_2 in run products varying from 1.2 to 2.1 log units below the IW buffer. The
340 low FeO content of experiment Fe_13 gives a much lower fO_2 of 4.4 log units below the IW
341 buffer. Experiments Fe_13 and Fe_14 used an Fe-free starting mix, and Fe_13 may have
342 failed to attain equilibrium between the Fe capsule and experimental charge (see below), so
343 this value is likely unreliable. The FeO content of melt in Fe_14 is higher and comparable to
344 experiments performed using the FeO-rich starting mix, suggesting that full equilibrium was
345 attained. Fe_14 was performed at 160°C higher temperature, providing an explanation as to
346 why this experiment achieved equilibrium and Fe_13 did not.

348 Calculations of fO_2 presented in Table 2 assume that the metal phase is pure Fe.
349 Compositions of exsolved Fe in run products were not determined here, although it is unlikely
350 that the material is pure Fe, and may contain variable amounts of O, Si, Cr and other elements.
351 The effect of such impurities on the calculation of fO_2 can be estimated using the model of
352 activity coefficients in liquid Fe metal by Wade and Wood (2005). The effect of adding
353 significant amounts (X=0.1) of Si, Cr etc to the Fe phase only results in an increase in
354 $\Delta log fO_2^{IW}$ of ≈0.1. As such, estimated fO_2 based on melt compositions in table 2 provides a
355 reasonable lower bound. As expected, values lie well within the range imparted by the sample
356 assembly (IW and Cr-Cr$_2$O$_3$ buffers). This range overlaps conditions assumed for lunar mantle
357 source regions, and allows us to assess the effect of reducing conditions on volatile
358 partitioning.

360 In contrast, Pt_C experiments do not contain a Fe-phase, and fO_2 cannot be estimated. The
361 absence of an Fe-rich phase in the experimental charge is consistent with a slightly higher fO_2
362 imparted from the sample assembly, i.e. fO_2 at approximately IW or higher. However, the
363 presence of an Fe-phase in experiments using Fe capsules might represent a dynamic
364 process of Fe dissolution at the edge of the capsule and exsolution of an Fe-rich solid within
365 the sample volume. Experiments Fe_13 and Fe_14 used Fe-free starting materials to test the
366 extent of equilibration between Fe capsules and run products. For the higher temperature
367 Fe_14, comparable Fe melt contents with other experiments strongly indicates attainment of
368 equilibrium, implying that exsolution of Fe in run products is not simply a transport process,
369 but a reflection of chemical equilibration under run conditions. Experiments Fe_6 and Fe_10,
370 which produced 100% melt with no evidence for the presence of crystalline (silicate) phases,
371 have melt FeO contents substantially lower than that of the Fe-rich starting composition used,
372 implying that melt FeO contents are, similarly, not simply reflective of the crystallisation of
373 more Fe-rich solid phases. Instead, melt composition is reflective of the equilibrium given in
374 [2]. Lack of exsolved Fe in Pt-C experiments implies more oxidising conditions above the IW
375 buffer. More broadly, capsule-sample exchange noted in experiments Fe_13 and Fe_14
376 supports attainment of equilibrium in experiments, aside from the FeO content in Fe_13.
377 Demonstrating chemical equilibrium in high pressure/temperature experiments is notoriously
378 difficult. However, the fact that experiments described here are performed at high
379 temperatures, have high melt fractions favouring melt-crystal exchange throughout
380 experimental charges, and that run products typically consist of euhedral, unzoned crystal
381 phases supports attainment of equilibrium, or at least development of steady state conditions.
382 Cr$_2$O$_3$ contents of run products are variable between experiments, although this likely reflects
383 variations in capsule morphology rather than disequilibrium.

384

385   Compositional data for quenched melt was obtained in regions distal from quench crystals,
386 but as close to analysed solid phases as possible. Aside from Fe_13, where Fe exchange with
387 the capsule did not reach equilibrium, Fe contents in all run products are variable, with melt
388 compositions ranging from 7.5 to 18.4 weight %. Fe_5 is the exception, where silicate melt
389 FeO content, 29.5%, exceeds that of the starting mix. Melt composition is additionally
390 dependent on phase relations, although in this experiment only olivine and quenched melt
391 where identified, and olivine has a similarly high FeO content. The reason for this discrepancy
392 cannot be fully explained. Olivine in Fe_4 is also relatively FeO rich and in equilibrium with
393 melt with a substantially lower FeO content. However, the lower temperature Fe_4 contains
394 additional orthopyroxene, which has a much lower FeO content. Higher FeO melt contents in
395 Fe_5 imply $\Delta \log fO_2^{IW} \approx -1.3$, which is less reducing than other experiments with Fe capsules.
396 As such, this may have resulted in net dissolution of FeO into the melt from the capsule, as
397 opposed to exsolution of variable Fe from the melt, as noted in other samples.

398

399   Melt in Pt_C experiments has FeO contents of 9.9 and 14.0 weight %, comparable to
400 experiments with Fe capsules. However, in this instance there is no obvious exsolution of Fe
401 metal from the experimental charge which might explain reduction in FeO content compared
402 to the starting bulk composition. Similarly, coexisting orthopyroxene in these experiments has
403 similarly low FeO. Fe loss to Pt is common in high pressure experiments, which might explain
404 observed compositions if parts of the experimental charge were in contact with the outer Pt
405 capsule. Although examination of run products suggests that inner graphite capsules retained
406 integrity, this possibility cannot be discounted. Alternatively, it is possible that the presence of
407 some additional Fe-rich phase, such as small quantities of a spinel-type phase, accounts for
408 lower than expected melt Fe contents. SEM examination of run products provides no evidence
409 for this, although the possibility cannot be discounted.

410

411   Phase relations in run products vary with experimental conditions and capsule type. For the
412 most reduced Fe-bearing experiments with Fe capsules, olivine comes onto the liquidus below
413 1550°C followed by orthopyroxene below 1400°C, with significant amounts of melt still present
414 (Figures 1B, C). This is broadly consistent with previous studies using low-Ti ultramafic lunar
415 glass bulk compositions at 2 GPa and under reducing conditions (e.g. Barr and Grove, 2013;
416 Chen and Lindsay, 1982; Chen et al., 1983; Elkins-Tanton et al., 2003). From experiment Fe_2
417 it is apparent that enrichment in Cr_2O_3 stabilises Cr-rich spinel in run assemblages, and
418 orthopyroxene at the expense of olivine. Previous studies indicate that clinopyroxene is
419 stabilised at lower temperatures, sometimes at the expense of olivine, and/or at slightly higher
420 pressures (e.g. Barr and Grove 2013; Elkins-Tanton et al., 2003). Indeed, the lowest
421 temperature (1340°C) experiment, Fe_13 which was run with an initial Fe-free bulk
422 composition that was then allowed to equilibrate with the Fe capsule did result in large
423 intergrowths of orthopyroxenes and pigeonite in equilibrium with the melt phase. In the higher
424 temperature 1500°C run for the same design, substantial reaction of the experimental charge
425 with the Fe capsule occurred, implying attainment of Fe saturated conditions during the
426 experiment. However, unlike the olivine+melt assemblage of run Fe_5 also at 1500°C, Fe_14
427 consisted of small pigeonite crystals disseminated throughout a glass/melt phase.
428 Stabilisation of pigeonite in these experiments might be due to Fe-Mg exchange in the run
429 products, and/or some effect of small variations in fO_2. An fO_2 dependence on melt relations
430 in more Ti-rich systems was noted by Krawczynski and Grove (2012) and Brown and Grove
431 (2015), due to its effect on Fe-Mg exchange, Ti valence and Fe-Ti coordination. In particular,

432 Brown and Grove (2015) noted that a decrease in fO_2 resulted in an increase in the multiple
433 saturation point, and stabilisation of pigeonite. As such, varying bulk Fe contents during
434 experiments here might explain the presence of pigeonite rather than olivine. An additional
435 complication here is the effect of run conditions on SiO_2 activity. Lower FeO abundance in
436 experiments results in an increase in the ratio $SiO_2/(FeO+MgO)$. An increase in this ratio could
437 conceivably stabilise pyroxene over olivine as a liquidus phase.
438
439 Experiments Pt_hal 1 and Pt_hal 2 were less reduced due to the use of graphite lined Pt
440 capsules. Run products contain smaller orthopyroxene crystals in equilibrium with a melt
441 phase instead of the liquidus olivine formed at more reduced conditions. Replacement of
442 orthopyroxene for olivine was noted by Barr and Grove (2013) as characteristic of higher-
443 pressure conditions. Given these experiments were consistently run at 2.0 GPa, a change in
444 phase relations instead implies some effect of capsule design. For Pt_C experiments, melt
445 FeO contents are again towards the lower range of compositions measured in this study. As
446 such, a similar effect of Si activity in lower FeO systems might stabilise pyroxene, and/or it is
447 again possible that fO_2 influences Fe (and Ti) coordination and phase stability. Melt H_2O
448 contents in Pt_C experiments are also higher than other experiments (Table 3), implying either
449 that water was better retained during these experiments or that H-related species in the more
450 reduced runs are less soluble in silicate melt. In this capsule design most water should be
451 retained in the experimental charge, although it is evident from stiffening of Pt that some H
452 diffuses into the outer capsule material. In contrast, with the Fe+Pt capsule design one might
453 expect H diffusion into the buffer mix to give lower 'water' contents in the melt. A difference in
454 melt 'water' content may also affect near-liquidus phase stability, as OH is a melt network
455 modifier.
456
457
458 **3.2 H_2O, F, Cl, and CO_2 composition data.**
459
460 F, Cl and H_2O contents of all phases are listed in Table 3. F and Cl contents of melts were
461 determined using both EMPA and SIMS. As shown in Figure 2 and Table 3, there is
462 reasonable consistency between SIMS and EMPA data. For F there is a general linear
463 correlation with some scatter. There is a consistent offset between SIMS and EMPA data such
464 that SIMS F contents are between 0.5 and 1 wt% higher. This could be related to a matrix
465 mismatch between these samples and the standards in SIMS analysis, although it might
466 equally relate to a systematic error arising from the EMP calibration. For Cl data, aside from
467 Pt_hal1, there is good consistency between SIMS and EMPA data and a close to 1:1 linear
468 correlation. When determining partition coefficients (concentration in mineral/concentration in
469 melt), SIMS melt data have been used. Cl and F contents of all mineral phases were below
470 the detection limit for EMPA, and H_2O contents cannot be determined by EMPA. Therefore,
471 use of only SIMS data for determining partition coefficients ensures consistency.
472
473 The loaded water content of all experiments at 2 wt% is well below saturation for the melt. H_2O
474 contents in mineral phases in all samples are subsequently low, from a few 10s to 100s ppm
475 by weight, compared to other fluid-saturated experiments. H_2O contents of melt are higher,
476 although significantly lower than the loaded 2 wt% in the Fe+Pt capsule runs (Table 3). This
477 implies that a significant fraction of 'H' is lost from charges during these experiments, possibly
478 relocated to the buffer capsule, but also into Fe and Pt capsule materials under reducing
479 conditions. This contrasts with the higher water contents in the Pt-C experiments. F and Cl

480 are also incompatible and concentrated in the melt phase, and measured concentrations
481 suggest no loss during the experiment. In fact, for samples Fe_6 and Fe_10, which are 100%
482 melt, F contents of the melt phase are higher than the starting composition. It cannot be
483 discounted that these experiments did produce small amounts of an additional solid phase not
484 observed in sections. However, this would also be explained by systematic over determination
485 in measured F by SIMS, or by weighing errors in starting mix preparation.

487 SIMS analysis of both mineral and melt in Fe capsule experiments suggests heterogeneous
488 distribution of small amounts of C, measured as CO_2 (Table 3). Fe capsule experiments are
489 nominally C-free. However, contamination of experimental charges during loading and during
490 preparation of starting mixes would provide a source for the detected C. C ingress from the
491 graphite furnace is another possibility (Brooker et al., 1998). For Pt-C experiments, the use of
492 an inner capsule results in graphite saturation and a ready source for C, C-O, C-H species
493 during experiments. CO_2 contents of melt in these experiments are notably higher.

495 Representative FTIR spectra obtained from glass and mineral phases are shown in Figure 3.
496 Glass spectra contain a broad, asymmetric absorption feature over the wavenumber range
497 3000-4000 cm^{-1} that is characteristic of O-H stretching. Absence of molecular H_2O bending
498 absorption bands at 1630 cm^{-1} and 5200 cm^{-1} suggests this species is largely absent,
499 consistent with the low total 'water' concentration (Stolper, 1982). Even under reduced
500 conditions, water is dominantly incorporated as OH^- in glass, either as isolated OH^- or as
501 clusters of OH^- groups, or in accordance with Cody et al. (2020), possibly even as H_2O. Only
502 one spectrum contains the broad absorption feature around 4000-4500 cm^{-1} which Kadik et
503 al. (2006) assigned to molecular H_2. This sample also has an unassigned broad feature at
504 2600 cm^{-1}. There is no H_2 specific calibration for silicate melt which would allow estimation of
505 an equivalent 'H_2O' content corresponding to the 4000-4500 cm^{-1} band, although it is likely
506 that the concentration of H_2 in Fe-10 glass is small in comparison with concentration of O-H.
507 This H_2 band is not noted in other spectra implying that H_2 is either absent or below detection
508 limit. Sample Fe_10 was synthesised at higher pressure than other samples (3 GPa compared
509 to 2 GPa) but still failed to display evidence of significant H_2. It might be expected that higher
510 pressure would stabilises a small proportion of 'water' as H_2, in accordance with Hirschmann
511 et al. (2012). Attempts to access conditions higher than 3 GPa resulted in a 100% failure rate
512 with this capsule design.

514 Spectra from large orthopyroxene crystals also show broad absorption features in the O-H
515 stretching frequency range 3000-3800 cm^{-1} (e.g. Stalder, 2004; Bromiley and Bromiley, 2006).
516 The double absorption feature between 2300-2400 cm^{-1} noted to varying degrees in all spectra
517 is due to failure to correct for atmospheric CO_2 within the spectrometer beam path. There is
518 no indication that this CO_2 is intrinsic to samples. Spectra do, however, contain multiple
519 absorption features around 2900 cm^{-1}. 3 distinct, sharp bands are noted in spectra,
520 reminiscent, although at slightly different wavenumbers, to a cluster of small, sharp absorption
521 bands which Kadik et al. (2006) assign to either CH_4 or C-H related species. Although samples
522 were re-cleaned in solvent, spectra still displayed these features. Despite this, it cannot be
523 discounted that these bands represent contamination from organic material, such as resin
524 used in sample preparation. Raman examination of quenched melt in samples Pt_hal1 and
525 Pt_hal2 (which could not be prepared as IR wafers) revealed the presence of a broad hump
526 at a Raman shift of approximately 3500 cm^{-1} due to OH^-, with no characteristic sharp
527 absorption band around 4100 cm^{-1} due to H_2. Raman spectra show no evidence for the

528   presence of C-H related species, despite the higher C content of these samples, although this
529   could be due to higher fO_2 imparted by this capsule design. As expected, higher fO_2 in these
530   experiments means that all 'water' is incorporated as OH^- in the melt. Any H and C related
531   species in the crystalline phases would be below the detection limit of Raman spectroscopy
532   in these samples.

533

534   F, Cl, H_2O and CO_2 mineral/melt partition coefficients ($D_{F/Cl/H2O/CO2}^{mineral/melt}$) calculated using
535   SIMS data are included in Table 3. Even for a limited dataset, D_{H2O}, D_F and D_{Cl} data show
536   promising consistency, except for sample Fe_13 which has a larger $D_{H2O}^{opx/melt}$ than other
537   samples. This is also the sample which has the most prominent C-H absorption bands in FTIR
538   spectra and a low bulk FeO content. In contrast, there is a much larger scatter for the
539    $D_{CO2}^{min/melt}$ data both within and between samples, with values also scattered around 1.
540   Although previous studies demonstrate that C can be incorporated into reduced silicate melts
541   (Kadik et al., 2006; Hirschmann et al., 2012; Ardia et al., 2013), it is likely that measured CO_2
542   contents here largely reflect contamination; therefore, CO_2 partitioning is not considered
543   further.

544

545

546   **4. Discussion**

547

548   **4.1 Controls on H_2O, F, and Cl mineral/melt partitioning in reduced lunar systems.**

549

550   Figure 4 shows F, Cl and H_2O partition coefficients from this and previous studies as a function
551   of temperature. This new data for reduced lunar conditions confirms all three volatiles are
552   incompatible, consistent with previous studies. There is a general trend $D_F>D_{H2O}>>D_{Cl}$, except
553   for limited olivine data, which suggest $D_{Cl}>D_{H2O}$. H_2O is slightly more incompatible than F for
554   all phases, but Cl is much more incompatible than F. This would be predicted based on the
555   significantly larger ionic radius of Cl relative to F, assuming similar incorporation mechanisms.
556   For F partition coefficients, pigeonite>orthopyroxene>>olivine, which is again consistent with
557   observed halogen partitioning in natural, terrestrial samples (Urann et al., 2017). For H,
558   pigeonite≥orthopyroxene>olivine, and for Cl, pigeonite>orthopyroxene=olivine. Data from
559   Hauri et al. (2006) is from reanalyses of experimental products from numerous previous
560   studies in terrestrial systems, under various conditions. Rosenthal et al. (2015) conducted
561   experiments using a model tholeiitic composition and either graphite-lined Pt capsules (similar
562   to experiments Pt-hal1 and Pt-hal2 here, but not with reduced starting mixes) or Fe-saturated
563   Pt capsules (more oxidising). Dalou et al. (2012) used model basaltic and peridotitic
564   compositions that were nominally H-free and more oxidised than this study, as their use of
565   graphite capsules probably buffered fO_2 between FMQ+1 and FMQ-2. Beyer et al. (2012)
566   performed experiments in simplified $CaO-MgO-Al_2O_3-SiO_2 \pm Na_2O$ systems using Pt capsules;
567   fO_2 was not controlled, but probably lay close to the more oxidising Ni-NiO (NNO) buffer
568   considered 'intrinsic' in solid-media apparatus (Stokes et al., 2019; Matjuschkin et al., 2015).
569   Joachim et al. (2015, 2017) also performed experiments in a simplified $CaO-Al_2O_3-MgO-SiO_2$
570   system under water absent and water present conditions, respectively, also under unbuffered
571   but presumably more oxidising conditions. O'Leary et al. (2011) performed experiments using
572   a natural high-Al_2O_3 basalt starting mix and nominally Al-free synthetic analogue, and used
573   olivine-Ni composite capsules with a Ni-NiO buffer. As such, comparison of experimental
574   partition coefficients demonstrates that fO_2 has little discernible influence on halogen or H_2O
575   partitioning, at least down to fO_2 of approximately IW-2 at these pressures. Importantly, this

576 implies that partitioning data from studies under model terrestrial conditions provide insight
577 into the behaviour of volatiles under lunar conditions.

578

579 Temperature has little effect on H_2O and halogen partitioning, except possibly for Cl. Joachim
580 et al. (2015) noted a temperature dependence of $D^{mineral/melt}_{Cl}$ in a simple model system.
581 However, the same study also noted a strong effect of temperature on F partitioning which is
582 not supported by examination of data across other studies (Figure 4). In Figure 5 there is a
583 clear correlation between D_F and D_{H2O}, (excluding sample Fe_13) as noted by Joachim et al.
584 (2017). There is a weaker correlation between D_F and D_{Cl}, and possibly also a correlation
585 between D_{Cl} and D_{H2O}. Joachim et al. (2017) suggested a negligible effect of H_2O on Cl
586 partitioning, and suggested that correlations between F and H_2O partition coefficients implied
587 the presence of clumped F and H defects in olivine, as proposed by Crepisson et al. (2014).
588 Olivine partitioning data in this study is too limited to test this, although from Figure 5 is it clear
589 that D_F and D_{H2O} are correlated across all data for olivine, orthopyroxene and pigeonite.

590

591 It has been repeatedly observed that H_2O pyroxene-melt partitioning, and possibly olivine-melt
592 partitioning is dependent on mineral Al_2O_3 content, and in particular, on the extent of Al
593 substitution into tetrahedral sites in mineral structures ($^{IV}Al^{3+}$) (e.g. Hauri et al., 2006; Tenner
594 et al., 2009; O'Leary et al., 2011). Figure 6 shows a broad trend of increasing $D^{pyroxene/melt}_{H2O}$
595 with increasing $^{IV}Al^{3+}$, consistent with previous studies. Data here fit this broad trend, implying
596 that a coupled substitution of Al^{3+} for tetrahedral Si^{4+} charge-balances H incorporation in ortho-
597 and clinopyroxene under relatively reducing conditions. The obvious out-lying sample is
598 Fe_13, the lower temperature experiment performed using an Fe-free starting mix. Either this
599 sample is not fully equilibrated, or low bulk Fe content has a marked influence on H_2O
600 partitioning. The effect of increasing $^{IV}Al^{3+}$ on $D^{clinopyroxene/melt}_F$ for data here is broadly in
601 accordance with the trend noted by O'Leary et al. (2011) in high and low alumina basalts.
602 Scatter in the wider dataset implies additional controls on F incorporation, although from
603 Figure 6 it is apparent that coupled substitutions involving Al^{3+} are also an important control
604 on F pyroxene-melt partitioning.

605

606 Mosenfelder and Rossman (2013a,b) similarly proposed that F incorporation in pyroxene is
607 coupled to both Al^{3+} and Fe^{3+} substitution onto tetrahedral sites, and to monovalent cation
608 substitutions onto the M2 site. No effect of mineral Fe content on F partitioning is noted here,
609 although this is expected due to the low fO_2 used which excludes the presence of Fe^{3+}.
610 However, we observe clear positive correlations between mineral F content and mineral TiO_2,
611 Al_2O_3, and Cr_2O_3 contents (Figure 7). Correlation between F (and H_2O) and TiO_2 across
612 mineral phases could indicate F incorporation via Ti-clinohumite/Ti-humite type planar defects,
613 although this is not supported by detailed TEM analysis (e.g. Joachim et al., 2015). However,
614 in these reduced conditions it is likely that a fraction of Ti is incorporated in pyroxenes as Ti^{3+},
615 consistent with XANES measurements which demonstrate that pyroxenes and olivine
616 equilibrated at similar fO_2 can contain up for 25% Ti as Ti^{3+} (Leitzke et al., 2018). Coupled Ti^{3+}
617 and OH^- defects have been noted in other nominally anhydrous minerals such as rutile and its
618 high-pressure polymorph TiO_2 (II) (Bromiley et al., 2004b; Bromiley and Hilairet, 2005) under
619 more oxidising, high-pressure conditions. As such, all trends in Figure 7 likely result from F
620 incorporation charge-balanced by M^{3+} substitutional defects, as discussed in detail in Dalou et
621 al. (2012). In agreement with Dalou et al. (2012) and Mosenfelder and Rossman (2013b) there
622 is also an additional weak correlation between mineral Na content and F. Correlations are
623 generally weaker for Cl due to greater scatter in a smaller data set. However, it is possible that

13

624 there is a similar correlation between $^{IV}Al^{3+}$ on $D^{clinopyroxene/melt}_{Cl}$ (Figure 6). It is difficult to assess
625 the extent to which Al-Si substitution into olivine could charge-balance F and Cl incorporation,
626 although a wider comparison of data (Figure 6) possibly supports a positive correlation
627 between olivine Al_2O_3 content and $D_F^{olivine/melt}$.

629 Both Dalour et al. (2012) and Urann et al. (2017) observed that melt polymerisation has an
630 effect of mineral-melt partitioning of F and to a lesser extent, Cl. Melt polymerisation can be
631 represented by the ratio of non-bridging oxygen to tetrahedral sites (NBO/T) using major
632 element melt data, and is included in Table 3 and compared to partition coefficients in Figure
633 8. Within scatter, D_F appears to generally decrease with increasing NBO/T in accordance with
634 previous studies, and there is a similar, stronger control of NBO/T on D_{H2O}. Any such
635 relationship in the Cl dataset is less clear.

637 In summary, fO_2 has no discernible influence on F, Cl and H_2O partitioning. Partition
638 coefficients for all 3 volatiles are broadly comparable between the reduced model lunar system
639 used here and model terrestrial systems under more oxidised conditions. Volatile
640 incorporation mechanisms are also similar, implying that 'water' is structurally incorporated in
641 silicate melt, pyroxenes and olivines dominantly as OH^-. Kadik et al. (2006) concluded that at
642 fO_2=IW-2.4 'water' in silicate melts is largely incorporated as OH^-, with H_2 and C-H groups
643 dominating at more reduced conditions, although their experiments were conducted at higher
644 pressure (4 GPa). Hirschmann et al. (2012) suggested that pressure significantly increases
645 the proportion of H_2 in silicate melts. It is possible that at more reducing conditions at higher
646 pressures, the proportion of H_2 in both mineral and melt phases increases, potentially
647 influencing H partitioning in some way yet to be explored. However, for fO_2 estimates for the
648 lunar interior, and at the relatively low pressures where melting is likely to have occurred, it
649 appears that most 'water' will be incorporated as OH^-.

4.2 Volatile redistribution during lunar magmatic processes

654 Partion coefficients can be used to estimate the volatile content in mantle source regions for
655 lunar volcanic products. For example, Zhang et al. (2019) used a batch melting calculation (4
656 and 8% partial melting of a lunar cumulate consisting of 50% olivine, 25% pigeonite and 25%
657 orthopyroxene) to estimate a source region for lunar volcanic glasses with 6-22 ppm H_2O. By
658 comparison, the water content of Earth's mantle is estimated to be 290 ppm, or 100 ppm for
659 the depleted uppermost mantle, implying significant depletion of 'water' in the Moon relative
660 to Earth (Zhang et al., 2019). The same calculation using average $D_{H2O}^{min/melt}$ values
661 determined here (excluding Fe_13) gives a slightly lower maximum H_2O content of the lunar
662 mantle of 15 ppm. Applying the same calculation to F and Cl contents of mare basalt olivine-
663 hosted melt inclusions of 34-77 and 1.7-3.0 ppm, respectively (Chen et al., 2015), gives lunar
664 mantle volatile contents of 2.4-8.4 ppm for F, and 0.07-0.3 ppm for Cl. For comparison, Ni et
665 al. (2019) estimated a lunar mantle source region based on melt inclusion data with H_2O of 84
666 ppm, F of 5 ppm and Cl of 0.39 ppm. Estimated terrestrial halogen contents are variable, as
667 recently summarised by Klemme and Stalder (2018), with proposed primitive mantle F and Cl
668 contents ranging from 18-25 ppm, and 1.4-35 ppm, respectively, depleted upper mantle F and
669 Cl contents ranging from 11-16 ppm, and 0.5-1 ppm, respectively, and bulk silicate Earth F
670 and Cl contents of approximately 15 ppm, and 17 ppm, respectively. As such, partitioning data
671 here imply a lunar mantle source region which is both significantly volatile-depleted relative to

672   the terrestrial mantle, and depleted in Cl relative to F and H_2O. As previously noted (e.g. Hauri
673   et al. 2015; McCubbin et al. 2015; Boyce et al., 2015), depletion of Cl compared to both F and
674   H_2O is characteristic of the lunar mantle.
675
676   As noted by McCubbin et al. (2015), however, calculation of lunar mantle volatile contents
677   from geochemical characteristics of volcanic products can give a misleading impression of
678   bulk lunar composition. The lunar mantle is likely heterogenous with respect to water and other
679   volatiles (McCubbin et al., 2015), and high volatile contents promote mantle melting. As such,
680   calculated volatile contents from mare basalt and volcanic glass data may not be
681   representative of the 'average' lunar mantle, and may be overestimates. Following accretion
682   of the Moon, cooling and progressive crystallisation of the Lunar Magma Ocean (LMO) would
683   have resulted in partitioning of F, Cl and H_2O between mantle cumulates and the remaining
684   magma. The incompatible nature of all three volatiles means that they would have been
685   increasingly concentrated in the final products of LMO solidification. Differences in
686   incompatibility may have also resulted in relative fractionation of F, Cl and H_2O. McCubbin et
687   al. (2015) argued that depletion of Cl relative to F and H_2O in lunar volcanics implies sourcing
688   from a lunar mantle whose composition largely reflects mineral-melt partitioning of volatiles
689   during LMO solidification.
690
691   Elkins-Tanton and Grove (2011) used published, i.e. 'terrestrial', H_2O partition coefficients to
692   model distribution of H_2O during LMO crystallisation, and suggested an initial LMO 'water'
693   content of approximately 1000 ppm H_2O. McCubbin et al. (2015) used published or estimated
694   partition coefficients for F, Cl and H_2O, corrected for varying mineral chemistry, to model
695   sequential solidification of the LMO using the crystallisation model of Elardo et al. (2015), and
696   constrained volatile concentration and relative fractionation. Here we adopt a similar
697   approach, incrementally solidifying a LMO over 100 steps using the crystallisation sequence
698   of Rapp and Draper (2018) (Table 4). At each step we use $D^{min/melt}$ values for H_2O, F and Cl
699   based on data from this study, and a fractional crystallisation calculation to determine volatile
700   contents in remaining magma and newly-formed cumulate (Table 4, and supplementary
701   material). McCubbin et al. (2015) derived models for the effect of $^{IV}Al^{3+}$ on volatile partition
702   coefficients to account for variations in $D_{H2O/F/Cl}$ due to changes in mineral chemistry during
703   the various stages LMO solidification. However, due to uncertainties in the correlations
704   between $D_{H2O/F/Cl}$ and $^{IV}Al^{3+}$, especially for Cl, and variations in $D_{H2O/F/Cl}$ due to other
705   compositional effects (including the extent of melt polymerisation), here we use specific
706    $D_{H2O/F/Cl}$ for samples with broadly similar compositions to those in the experiments of Rapp
707   and Draper (2018). $D_{H2O/F/Cl}^{olivine/melt}$ are taken from Fe_5. During comparable stage 1
708   experiments, Rapp and Draper (2018) note variations in olivine composition from Al_2O_3 of
709   0.04-0.13 wt%, compared to 0.1 wt% for olivine in Fe_5. Orthopyroxene $^{IV}Al^{3+}$ varies from 0.08
710   to 0.128 apfu in experiments here, overlapping compositions for orthopyroxene in stage 2
711   (0.096-0.124) in experiments of Rapp and Draper (2018). Therefore, for stage 2 we use
712   average D values for orthopyroxene from experiments here, not including Fe_13. For stage 3,
713   orthopyroxene in experiments of Rapp and Draper (2018) is slightly more aluminous, with
714    $^{IV}Al^{3+}$ varying from 0.128-0.184. Any increase in $D^{orthopyroxene/melt}$ for F and H_2O due to this
715   increase in $^{IV}Al^{3+}$ is small, and possibly minor compared to other compositional changes.
716   Furthermore, because of a lack of data on how $D^{orthopyroxene/melt}$ varies for Cl we use the same
717   partition coefficients as used for stage 2. $D_{H2O/F/Cl}^{clinopyroxene/melt}$ are taken from Fe_14.
718   Clinopyroxene $^{IV}Al^{3+}$ for this sample is 0.14, and CaO content 16.6 wt%, compared to $^{IV}Al^{3+}$
719   =0.18 and CaO=13.45 wt% for clinopyroxene in stage 3 crystallisation experiments of Rapp

and Draper (2018). For plagioclase we use an average $D_{H2O}^{plag/melt}$ from Lin et al. (2019), who measured H_2O partitioning between plagioclase and melt in a model lunar system. Due to a lack of data on plagioclase/melt partitioning of F and Cl, and the similarity of H_2O partition coefficients for plagioclase from Lin et al. (2019) to pigeonite data here, we use pigeonite Cl and F partition coefficients to tentatively model plagioclase-melt partitioning. Rapp and Draper (2018) note formation of an intermediate Ca-content plagioclase during stage 4 experiments, with $^{IV}Al^{3+}$ = 0.05 to 0.09. To model crystallisation of this phase we use orthopyroxene partitioning data from Pt_hal1 ($^{IV}Al^{3+}$ =0.08).

LMO solidification was modelled up to 97% crystallisation. Later stages of crystallisation involve formation of more complex cumulate assemblages, including mineral phases for which no partitioning data is available. Furthermore, the effect of progressive increases in melt polymerisation are not considered here; these may have a considerable influence during the latter stages of LMO solidification. The purpose of modelling here is, instead, to test the extent to which new data allow trends in volatile abundance in LMO cumulates to be identified. There are, however, two additional complications in using such an approach to model lunar mantle volatile abundances. Firstly, cumulates formed during LMO solidification will contain a proportion of trapped liquid. Elkins-Tanton and Grove (2011) argued for a proportion of trapped intercumulate liquid (ICL) of 5-10%, which would have a strong influence on bulk cumulate incompatible element chemistry. Given that all volatiles are highly incompatible, this degree of liquid retention would dominate cumulate volatile content. McCubbin et al. (2015) argue that because of this, geochemical observations imply that the amount of intercumulate liquid (ICL) was likely low (below 1%). Here, we model ICL contents of 0 and 1% using the approach of McCubbin et al. (2015), by instantaneously trapping liquid at each stage of cumulate formation.

An additional complication is cumulate overturn and hybridisation during the latter stages of LMO solidification, which acts in effect to partially homogenise the lunar mantle (Shearer et al., 2006). One important effect of cumulate overturn is partial melting within overturned, hybridised cumulates, resulting in formation of mare basalts and associated volcanic products. As such, regions of the lunar interior 'sampled' by volcanic activity have any signature of LMO solidification 'overprinted' by cumulate overturn and associated processes. Despite this, modelling progressive crystallisation provides insight into the distribution of volatiles in the products of LMO solidification, including various cumulate sequences and later stage liquids (>99% crystallisation) which eventually form a proposed urKREEP component enriched in volatiles (Taylor et al., 2006).

To model the effects of LMO crystallisation on volatile distribution we use bulk silicate moon (BSM) volatile estimates from McCubbin et al. (2015). These are based on their LMO crystallisation model and estimates for the proportion of residual liquid trapped within cumulates formed during LMO solidification. LSHA* is a BSM composition which McCubbin et al. (2015) derive from modelled F abundances in lunar soil and highlands apatite. This BSM composition has an upper volatile content of 13.1 ppm H_2O, 7.1 ppm F and 13.8 ppm Cl. CFHA* is a BSM composition which McCubbin et al. (2015) derive from CI chondritic and highlands apatite F abundances. This BSM has upper volatile concentrations of 114 ppm H_2O, 60 ppm F and 123 ppm Cl. As such, these models provide volatile-poor and relatively volatile-rich estimates of bulk lunar composition, although with a markedly lower H_2O content than that proposed by Elkins-Tanton and Grove (2011).

768 Figure 9 shows the results of LMO solidification modelling using the CFHA* BSM composition
769 (additional information, and results using both CFHA* and LSHA* compositions is given in
770 supplementary material). All three volatiles are highly incompatible, and as expected early
771 formed cumulates are essentially volatile-free. Once orthopyroxene crystallises and
772 solidification exceeds 60% there is a marked increase in cumulate volatile content, and
773 importantly, a marked change in volatile ratios (Figure 6C). The slightly higher compatibility of
774 F means that, despite overall volatile concentrations, F/H_2O in cumulate is initially >2, but
775 following formation of pyroxene-rich cumulates, decreases sharply, and stays at slightly above
776 1 during latter stages of LMO solidification. Formation of pyroxene also results in a marked
777 increase in the ratio F/Cl, which approaches 3 during latter stages of LMO solidification.
778 Addition of inter-cumulate liquid (ICL) masks these signatures of mineral-melt partitioning.
779 However, even the addition of 1% ICL still results in marked trends in F/H_2O, which increases
780 to 0.8 during LMO solidification, and F/Cl which approaches 1.
781
782 Results of modelling are in good agreement with McCubbin et al. (2015), despite differences
783 in approach used. Cumulate volatile contents are low and largely dependent on the original
784 LMO composition, but with enrichment of F relative to H_2O and F relative to Cl within
785 cumulates. During latter stages of LMO solidification volatiles contents of cumulates approach
786 a few 10s ppm for a CFHA* composition, and a few ppm for a LSHA* composition, even with
787 additional 1% ICL. As such, regardless of differences in LMO crystallisation sequence used,
788 or in choice of partition coefficients and the dependence of these on composition, there are
789 clear trends arising from LMO solidification. For low estimates of the extent of trapped
790 intercumulate liquid, lunar mantle cumulates are enriched in F relative to Cl, and in F relative
791 to H_2O compared to the original LMO composition. As all volatiles are highly incompatible
792 there is, correspondingly, a marked increase in volatile content of remaining liquid during LMO
793 solidification (Figure 9A), which approaches 1000s ppm for each when the CFHA* composition
794 is used, and 100s ppm for each with an LSHA* composition (supplementary material).
795 However, there are only relatively minor changes in volatile ratios in the liquid, even during
796 the latter stages of LMO solidification (Figure 6F). F/H_2O and F/Cl both remain close to 0.5,
797 reflecting the original composition of the LMO.
798
5. Implications for volatiles in the early Earth-Moon system.
799
800
801 New partitioning data for H_2O, Cl and F presented here demonstrate that volatile incorporation
802 in a reduced, model lunar system is comparable to more oxidised, terrestrial systems. At fO_2
803 down to approximately IW-2, H remains dominantly incorporated in nominally anhydrous
804 mantle minerals as OH^-, at least at relatively low pressures of the lunar interior. Comparison
805 of limited F, Cl and H_2O mineral-melt partitioning data demonstrates that all three volatiles are
806 highly incompatible, although F is slightly less incompatible, and Cl considerably more
807 incompatible. Incorporation of all three volatiles is likely coupled to substitution of other minor
808 elements in mantle minerals, and likely dependent on melt composition and structure.
809
810 New partitioning data supports previous work where coefficients from model and actual
811 terrestrial systems are used to investigate volatile behaviour during lunar processes. Partition
812 coefficients can be used to estimate volatile content of lunar mantle source regions from, for
813 example, melt inclusion data. Results are consistent with estimates based on incompatible
814 element ratios, implying a lunar interior which is depleted in volatiles relative to BSE, and
815 importantly, strongly depleted in Cl relative to F. Forward modelling of LMO solidification using

816 new partitioning data supports the model of McCubbin et al. (2015). Cumulate phases have
817 elevated F/H$_2$O and F/Cl relative to the original LMO composition, although the extent of any
818 signature is dependent on the proportion of intercumulate liquid trapped during solidification.
819 McCubbin et al. (2015) argue that a clear signature of Cl depletion in lunar material is
820 consistent with a lunar mantle volatile abundance largely dependent of mineral-melt
821 partitioning, implying low proportions of intercumlate liquid. However, although the lunar
822 mantle can have an elevated F/Cl inherited from LMO solidification, mineral-melt partitioning
823 is unable to fully account for the elevated F/Cl of lunar materials compared to chondritic and
824 terrestrial abundances (Hauri et al., 2015).

825

826

827

828

829 **Acknowledgements**

837

838

839   Table 1. Target model lunar compositions used for partitioning experiments. Target
840   composition is an Apollo green glass composition based on average glass bead analyses by
841   Saal et al. (2008), but discounting K and P.
842

Oxide	Saal et al. (2008)*	Volatile free mix	Volatile-bearing mix
SiO_2	45.67	45.59	44.07
TiO_2	0.40	0.40	0.38
Al_2O_3	7.79	7.77	7.52
Cr_2O_3	0.63	0.63	0.61
FeO	19.75	19.72	19.06
MgO	16.81	16.78	16.22
MnO	0.27	0.27	0.26
CaO	8.73	8.72	8.42
Na_2O	0.12	0.12	0.12
K_2O	0.01	0.00	0.00
P_2O_5	0.02	0.00	0.00
H_2O			1.98
F_2			0.58
Cl_2			0.78
Total	*100.21*	*100.00*	*100.00*

843
844

845 Table 2: Experimental conditions and run products (successful runs only). Key: opx=orthopyroxene (low Ca pyroxene), Cr-sp=Cr-rich spinel
846 (due to buffer contamination), melt=quenched melt/glass, ol=olivine, pig=pigeonite.
847

Run.	Capsule	Initial T (°C)	Final T (°C)	Pressure (GPa)	Duration (h)	Log fO$_2$ range constrained from assembly[2]	Estimated experimental log fO$_2$ [3]	Products
Fe_2	Fe+Pt foil	1500	1350	2	24	0 to -5.0	-2.1	opx+Cr-sp+melt
Fe_4	Fe+Pt	1500	1400	2	24	0 to -4.8	-1.7	ol+opx+melt
Fe_5	Fe+Pt		1500	2	24	0 to -4.4	-1.3	ol+melt
Fe_6	Fe+Pt		1550	2	24	0 to -4.2	-2.1	melt
Fe_10	Fe+Pt		1500	3	24	-0 to 4.4	-2.5	melt
Fe_13[1]	Fe+Pt		1340	2	24	0 to -5.0	(-4.4)	opx+pig+melt
Fe_14[1]	Fe+Pt		1500	2	24	0 to -4.4	-2.0	pig+melt
Pt_hal1	Pt_C		1500	2	72	-1 to +2	-	opx+melt
Pt_hal2	Pt_C		1450[4]	2	72	-1 to +2	-	opx+melt

848
849 [1] Starting mix is Fe-free but Fe is gained from the capsule
850 [2] Relative to Fe-FeO (IW) buffer based on Fe capsule and Cr-Cr$_2$O$_3$ buffer, or estimated for use of graphite inner capsule.
851 [3] relative to IW, determined from FeO content of silicate melt in equilibrium with Fe metal (see text for details).
852 [4] Thermocouple failure during experiment, estimated temperature based on transformer output (±30°C)

Table 3. Compositions of run products determined by electron microprobe and SIMS and corresponding mineral-melt partition coefficients.

	Fe_2		Fe_4			Fe_5		Fe_6	Fe_10
	melt	*opx*	*melt*	*ol*	*opx*	*melt*	*ol*	*melt*	*melt*
[1]n=	4/4/9	5/4/5	5/4/10	1/-/4	5/5/8	4/4/9	4/4/7	6/6/11	4/4
EMP data (wt%)									
Na_2O	0.41(3)	0.03(1)	0.27(2)	n.d.	0.02(0)	0.21(2)	n.d.	0.23(2)	0.24(2)
Al_2O_3	9.82(27)	3.58(55)	9.11(22)	0.12(3)	3.88(55)	7.43(28)	0.10(0)	7.94(19)	8.06(12)
FeO	11.30(43)	11.55(74)	18.44(29)	22.35(172)	13.93(74)	29.48(32)	28.86(71)	11.71(14)	7.52(24)
MgO	11.71(28)	27.52(75)	14.77(15)	38.76(150)	26.74(75)	13.79(24)	34.36(37)	17.48(10)	18.26(26)
CaO	13.88(20)	1.83(6)	9.37(19)	0.21(1)	1.39(6)	7.29(15)	0.22(0)	7.94(9)	8.24(4)
SiO_2	43.72(63)	53.35(66)	42.75(33)	37.77(22)	52.49(66)	38.65(41)	36.91(15)	44.51(65)	46.37(49)
Cr_2O_3	3.02(1)	3.03(23)	1.56(1)	1.00(5)	1.96(16)	0.52(0)	0.30(1)	7.18(40)	6.10(17)
TiO_2	0.72(1)	0.09(3)	0.56(1)	0.01(0)	0.07(1)	0.42(1)	0.01(0)	0.43(1)	0.44(1)
MnO	0.31(1)	0.22(3)	0.30(1)	0.22(1)	0.20(1)	0.24(1)	0.18(1)	0.26(1)	0.24(1)
F	3.88(31)	-	2.41(19)	-	-	1.71(11)	-	2.19(21)	2.27(4)
Cl	2.35(23)	-	0.83(1)	-	-	1.05(1)	-	1.17(1)	0.93(1)
Total	99.47(169)	101.20(35)	99.46(138)	100.44(45)	100.69(30)	100.52(103)	100.94(54)	101.25(60)	98.67(56)
NBO/T^2	1.44		1.65			2.08		1.83	1.61
Al_T (pfu)		0.110			0.123				
SIMS data (ppm)									
H_2O	2230(130)	39(12)	4120(170)	-	63(8)	3840(150)	4(4)	1410(80)	1230(150)
CO_2	25(5)	30(10)	19(2)	-	20(3)	27(23)	18(5)	41(38)	37(5)
F	53800(1500)	1240(120)	37500(1600)	160(-)	1048(58)	27460(690)	98(16)	30500(2400)	28100(900)
Cl	28180(880)	38(5)	9400(640)	n.d	41(22)	11470(550)	34(14)	12220(1120)	9100(260)
Mineral/melt partition coefficients[3]									
$D_{min/melt}^{H}$		0.018(6)		-	0.015(2)		0.0011(10)		
$D_{min/melt}^{F}$		0.023(2)		0.004(0)	0.028(2)		0.0036(1)		
$D_{min/melt}^{Cl}$		0.001(0)		-	0.004(0)		0.003(0)		
$D_{min/melt}^{C}$		1.25(49)		-	1.06(18)		0.67(59)		

	Fe_13			Fe_14		Pt_hal1		Pt_hal2	
	melt	*opx*	*pig*	*melt*	*pig*	*melt*	*opx*	*melt*	*opx*
[1]n=	4/3	4/3/6	2/2/2	5/5	1/1/4	5/4/4	5/4/5	4/4/12	5/54
EMP data									
Na_2O	0.33(5)	0.02(1)	0.20(1)	0.32(5)	0.23(1)	0.45(2)	0.03(1)	0.35(4)	0.02(0)
Al_2O_3	15.42(21)	3.68(108)	10.79(56)	13.16(13)	7.29(59)	10.52(19)	4.11(110)	10.27(2)	2.89(27)
FeO	0.83(17)	1.81(30)	0.59(3)	12.69(28)	4.77(180)	12.97(67)	14.00(0.38)	8.96(26)	9.91(124)
MgO	8.03(11)	32.65(157)	15.95(44)	7.30(13)	17.50(96)	11.45(18)	26.79(53)	15.05(13)	30.06(34)
CaO	12.51(12)	1.23(26)	13.47(92)	12.12(13)	16.55(192)	14.20(17)	1.63(10)	11.39(12)	1.14(5)
SiO_2	50.25(41)	54.99(138)	50.89(90)	46.43(40)	50.85(90)	41.62(81)	52.31(113)	44.22(45)	54.21(39)
Cr_2O_3	4.09(10)	0.15(4)	7.31(60)	0.58(2)	1.61(30)	0.18(1)	1.14(9)	0.35(0)	0.98(16)
TiO_2	0.49(1)	0.15(4)	0.57(2)	0.66(2)	0.30(3)	0.79(4)	0.07(1)	0.53(0)	0.05(1)
MnO	0.21(0)	0.27(4)	0.37(4)	0.19(1)	0.26(3)	0.28(1)	0.22(2)	0.23(1)	0.18(1)
F	4.95(8)	-	-	4.27(8)	-	3.92(5)	-	2.97(7)	-
Cl	1.08(1)	-	-	0.97(1)	-	2.87(5)	-	2.08(1)	-
Total	98.26(45)	99.82(54)	100.15(59)	98.73(32)	99.34(76)	99.33(36)	100.30(64)	96.28(78)	99.43(53)
NBO/T[2]	0.65			0.89		0.93		1.31	
Al_T (pfu)[3]		0.09	0.136		0.141		0.128		0.08
SIMS data									
H_2O	660(10)	61(32)	44(21)	4400(590)	144(-)	10200(670)	156(16)	28300(500)	287(40)
CO_2	61(23)	69(1)	81(9)	33(0)	n.d.	122(50)	50(0)	2986(62)	47(3)
F	48300(3400)	1383(58)	-	47000(5400)	3397(-)	31300(2800)	1160(125)	29500(100)	689(136)
Cl	8500(670)	69(1)	-	9000(1500)	70(-)	11000(1000)	40(9)	20300(800)	39(9)
Mineral/melt partition coefficients[3]									
$D_{min/melt}^H$		0.09(5)	0.07(3)		0.033(5)		0.015(2)		0.010(1)
$D_{min/melt}^F$		0.029(2)	-		0.072(8)		0.037(5)		0.016(4)
$D_{min/melt}^{Cl}$		0.003(0)	-		0.008(0)		0.004(0)		0.002(0)
$D_{min/melt}^C$		1.13(42)	1.3(5)		-		0.41(17)		0.016(1)

857   [1]Number of analysis for SIMS (F+Cl) /SIMS (H+C)/ EMP (major elements), one analysis per crystal;

858   [2]ratio of non-bridging oxygens to tetrahedral sites as a measured of melt polymerisation;

859   [3]Calculated atoms of Al on the tetrahedral site in pyroxene (per formula unit);

860   [4]Based on melt SIMS data.

861 Table 4: input data used to model volatile distribution during lunar magma ocean solidification. Steps during solidification and phase
862 assemblages are from Rapp and Draper (2018).
863

Stage/% solidifiction	Phase assembly (mineral proportions)	$D^{ol/melt}$			$D^{opx/melt}$			$D^{cpx/melt}$			$D^{plag/melt}$		
		H_2O	Cl	F	H_2O	Cl	F	H_2O	Cl	F	H_2O	Cl	F
1 (0-52%)	ol	0.001	0.003	0.004	-	-	-	-	-	-	-	-	-
2 (52-74%)	opx	-	-	-	0.015	0.002	0.03	-	-	-	-	-	-
3 (74-88%)	0.3 ol + 0.15 cpx + 0.15 opx + 0.4 plag	0.001	0.003	0.004	0.015	0.002	0.03	0.03	0.007	0.08	0.03	0.007	0.08
4 (88-97%)	0.6 opx + 0.4 plag	-	-	-				-	-	-	0.03	0.007	0.08

864
865
866

867   Figure 1. Backscattered electron images (SEM) of selected run products.
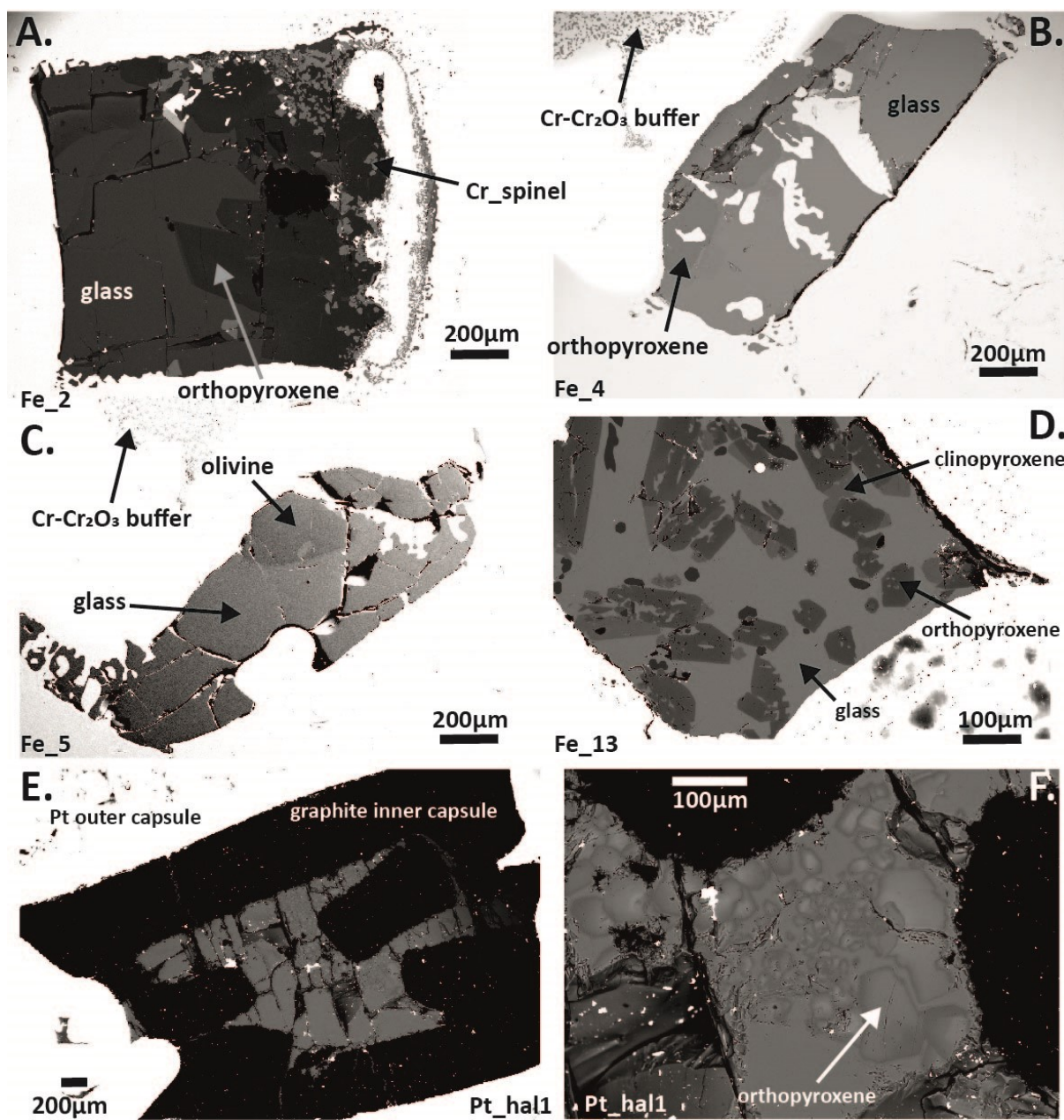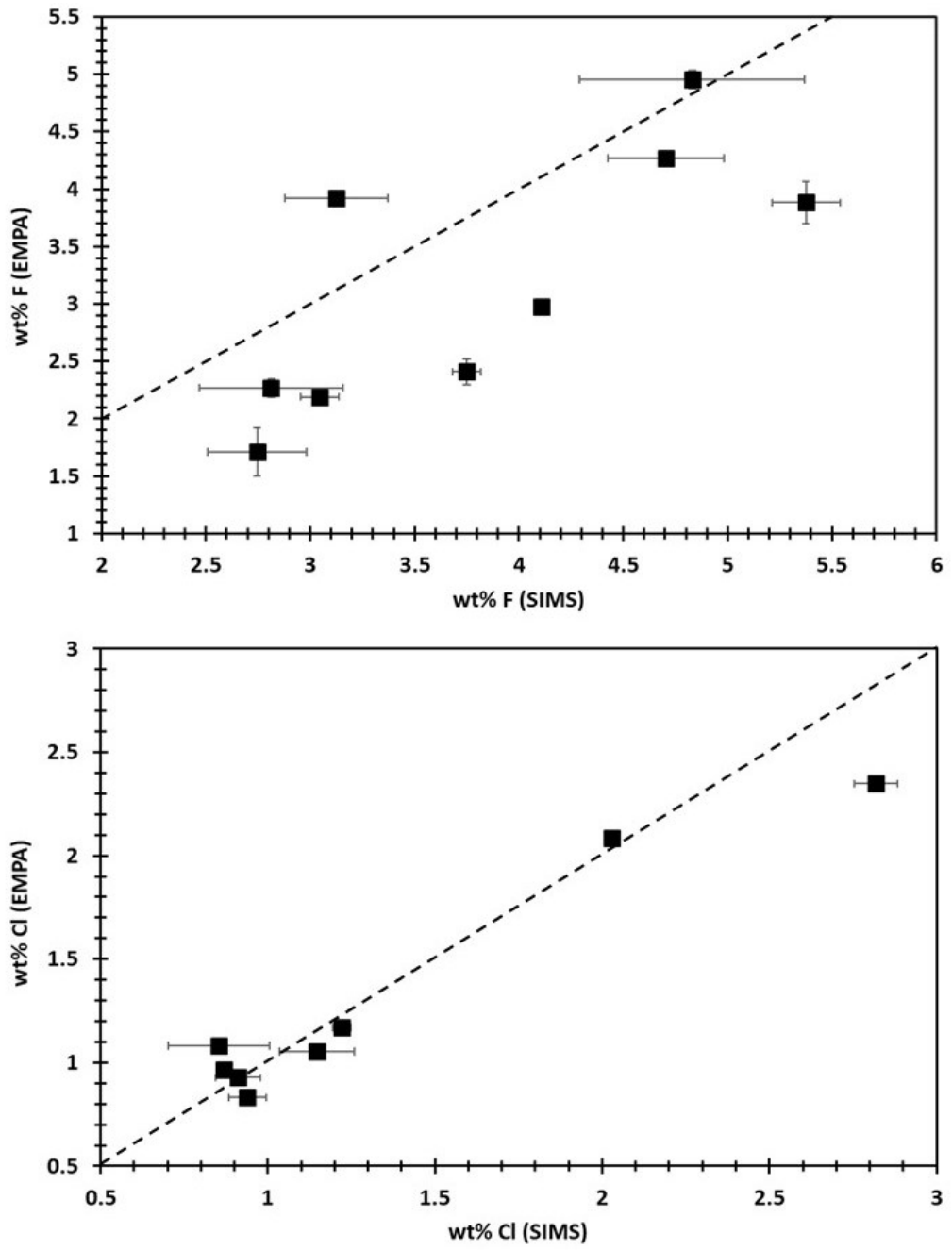

868
869
870

871   Figure 2: Comparison of SIMS and EMPA data for F (top) and Cl (bottom) concentrations in
872   glass (quenched melt). Error bars are standard deviations on mean values for each sample
873   based on repeat analyses. Dashed lines are 1:1 relationships.

874

875
876

Figure 3. Unpolarised FTIR spectra from selected run products, offset vertically for clarity,
878   and obtained from samples with consistent thicknesses, although not thickness corrected.
879   No background correction has been applied due to complex and contrasting backgrounds.

880

881

882

26
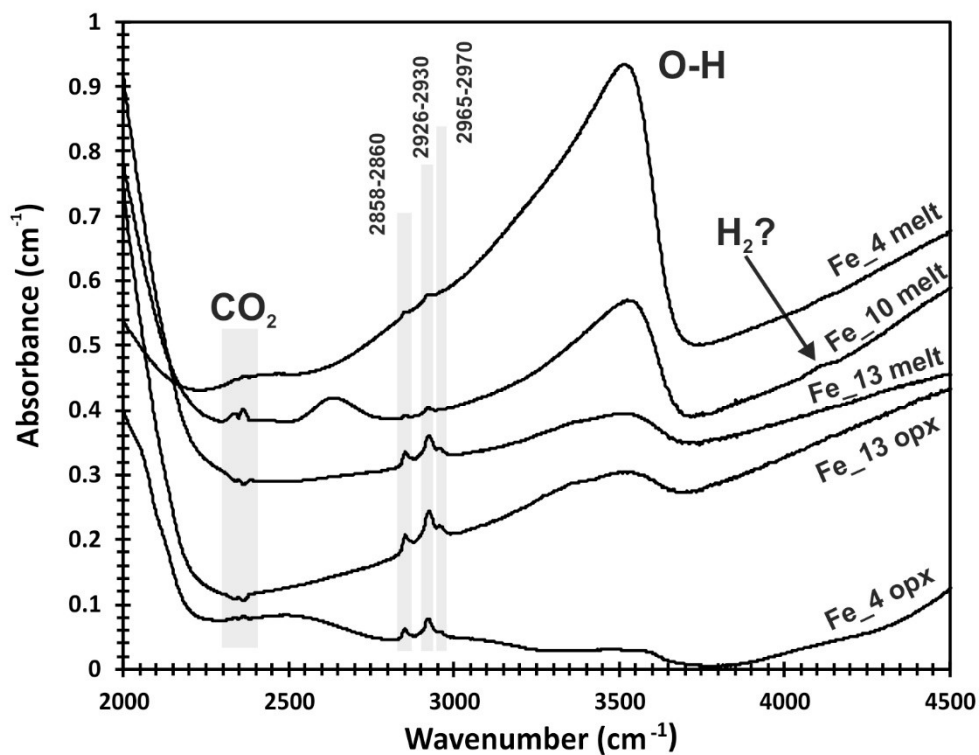
883 Figure 4. Effect of temperature on F, H_2O and Cl partitioning between silicate melt and orthopyroxene (squares), pigeonite/clinopyroxene (high
884 Ca pyroxenes) (circles) and olivine (triangles). Black symbols: this study, Grey: Hauri et al. (2006), Red: Joachim et al. (2017), Yellow: Joachim
885 et al. (2015), White: Rosenthal et al. (2015), Blue: Beyer et al. (2012), Hatched: Dalou et al. (2012), Green: O'Leary et al. (2010).

886
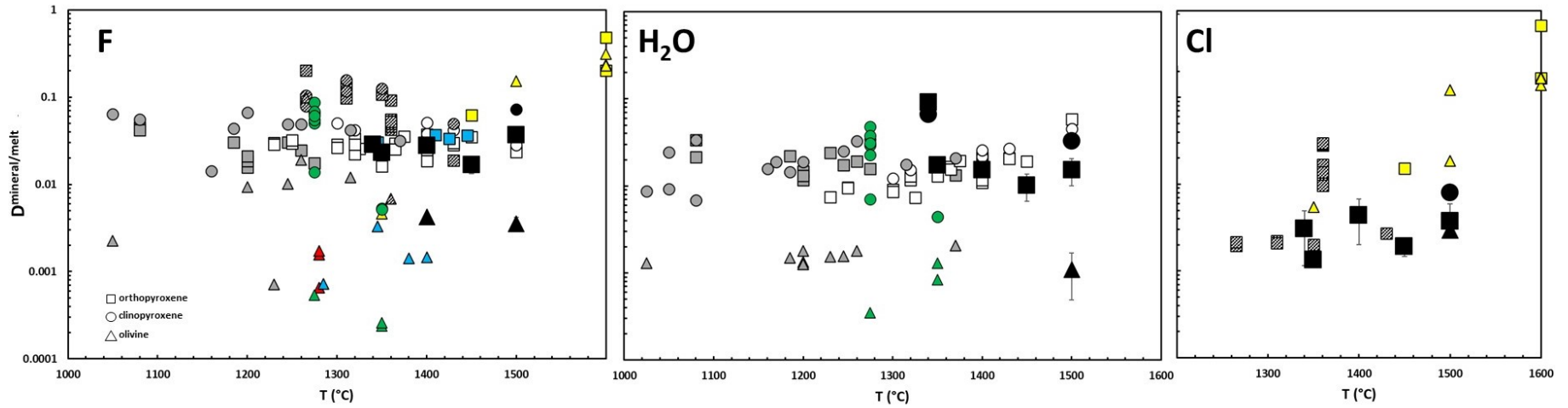
887

888   Figure 5. Relationship between F and H_2O mineral-melt partition coefficients (top) and Cl
889   and F partition coefficients, with relationship between Cl and H coefficients shown in insert).
890   Key as for Figure 4.

891

892

28
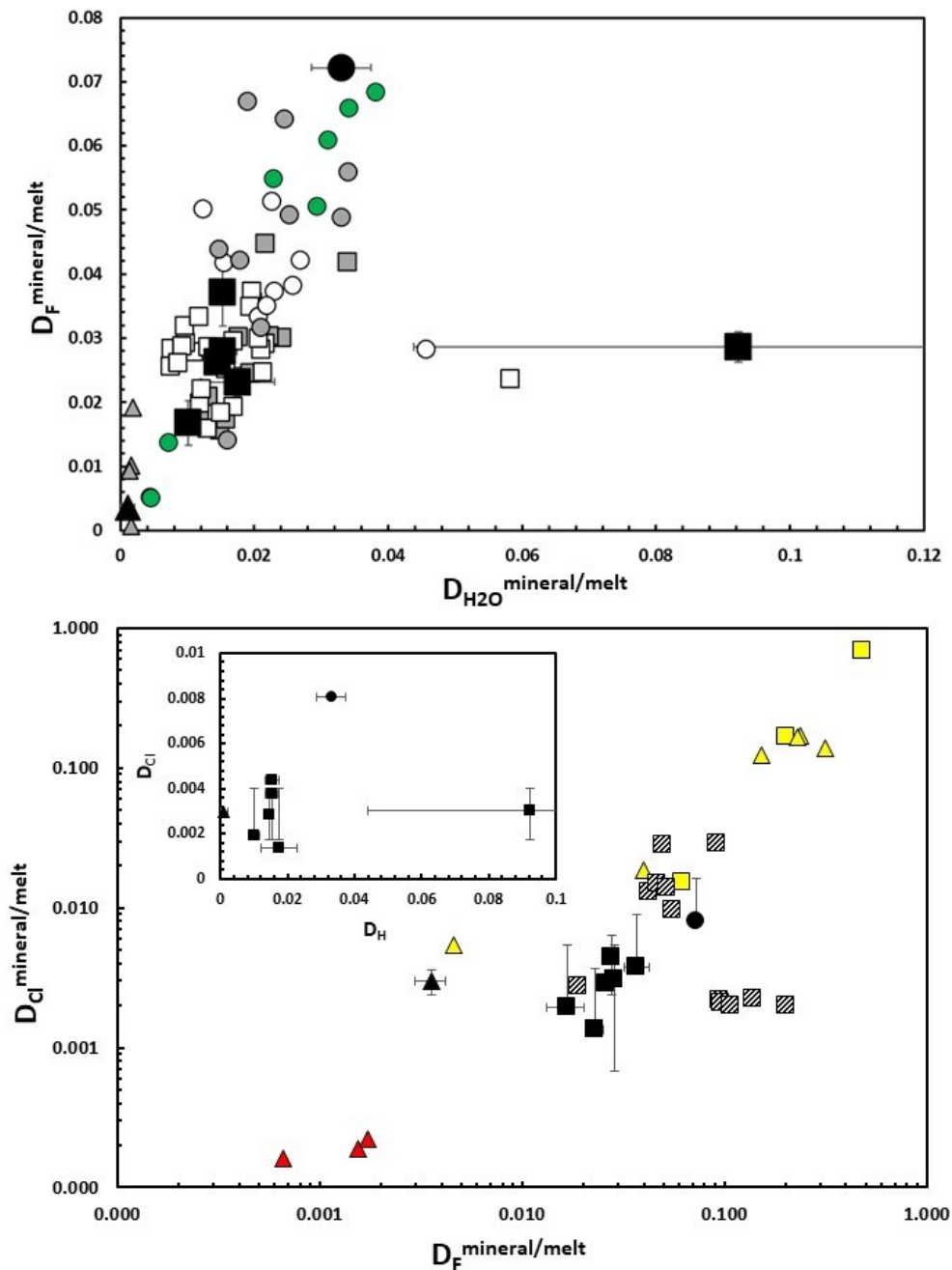
893   Figure 6. Top: F, H_2O and Cl pyroxene-melt partition coefficients as a function of atoms per formula unit (APFU) Al^{3+} on the tetrahedral site in
894   ortho- and clinopyroxene structures. Bottom: F and Cl olivine-melt partition coefficients as a function of olivine Al_2O_3 content (ppm by weight).

895

896

29
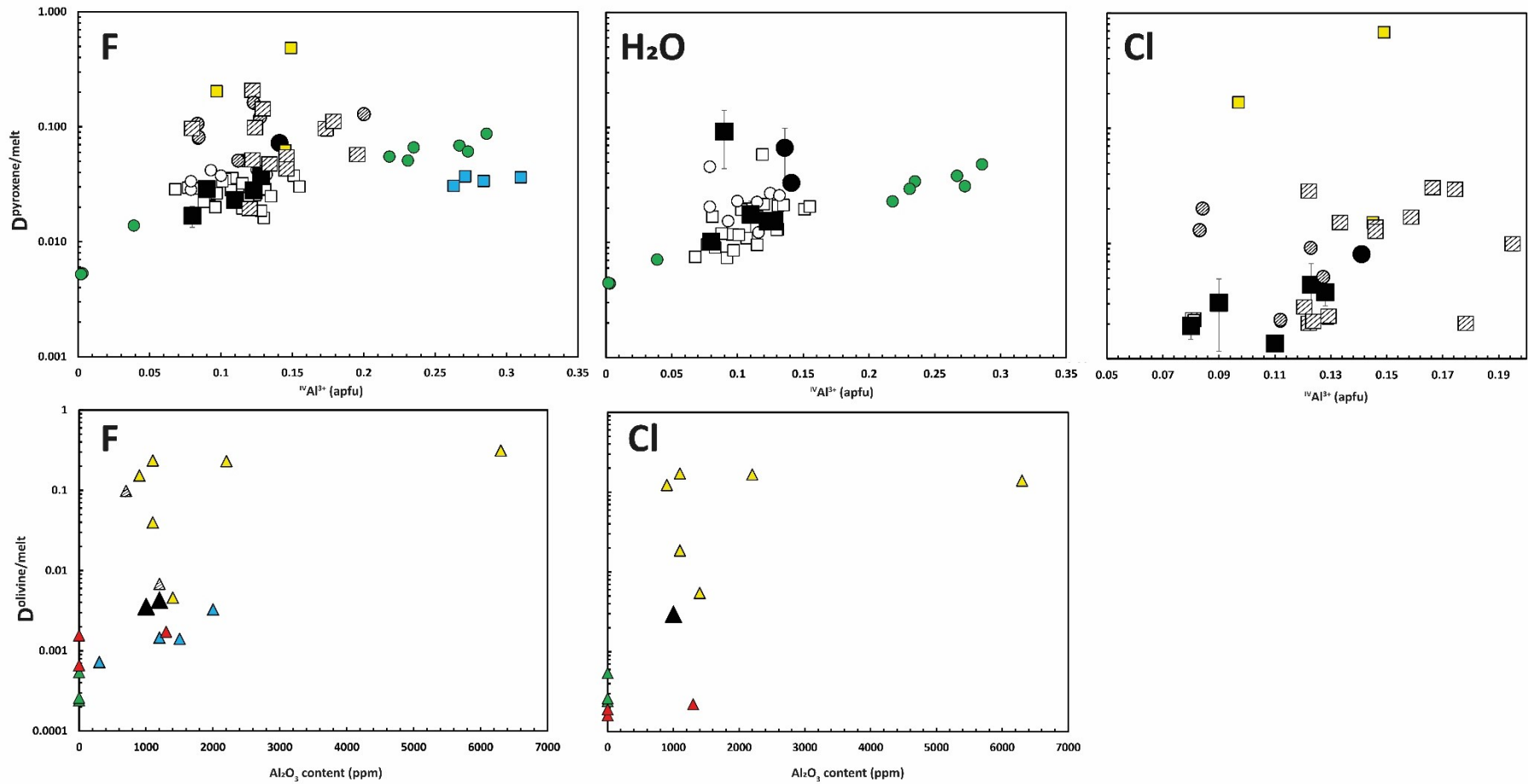
897   Figure 7. Variation in F content in minerals (measured by SIMS) with mineral chemistry
898   determined by EMPA (TiO$_2$ contents x10 for clarity).
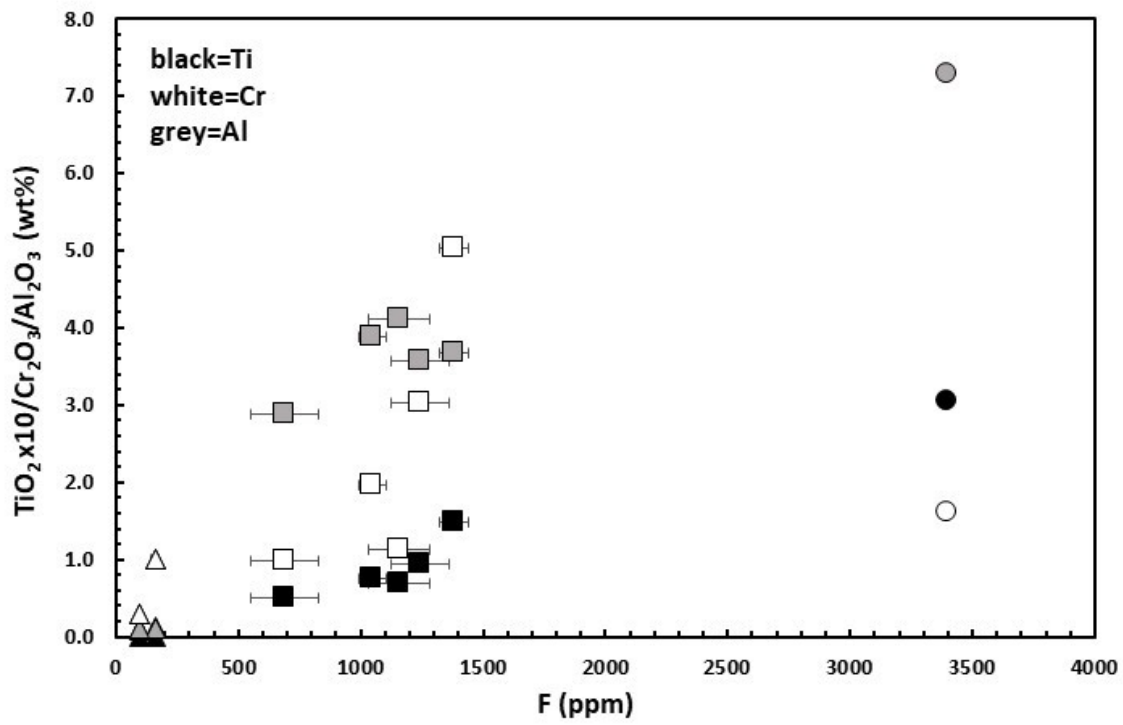
899

900

901   Figure 8. Effect of melt polymerisation, defined by the calculated ratio NBO/T, on volatile
902   partitioning. Key as for Figure 4.
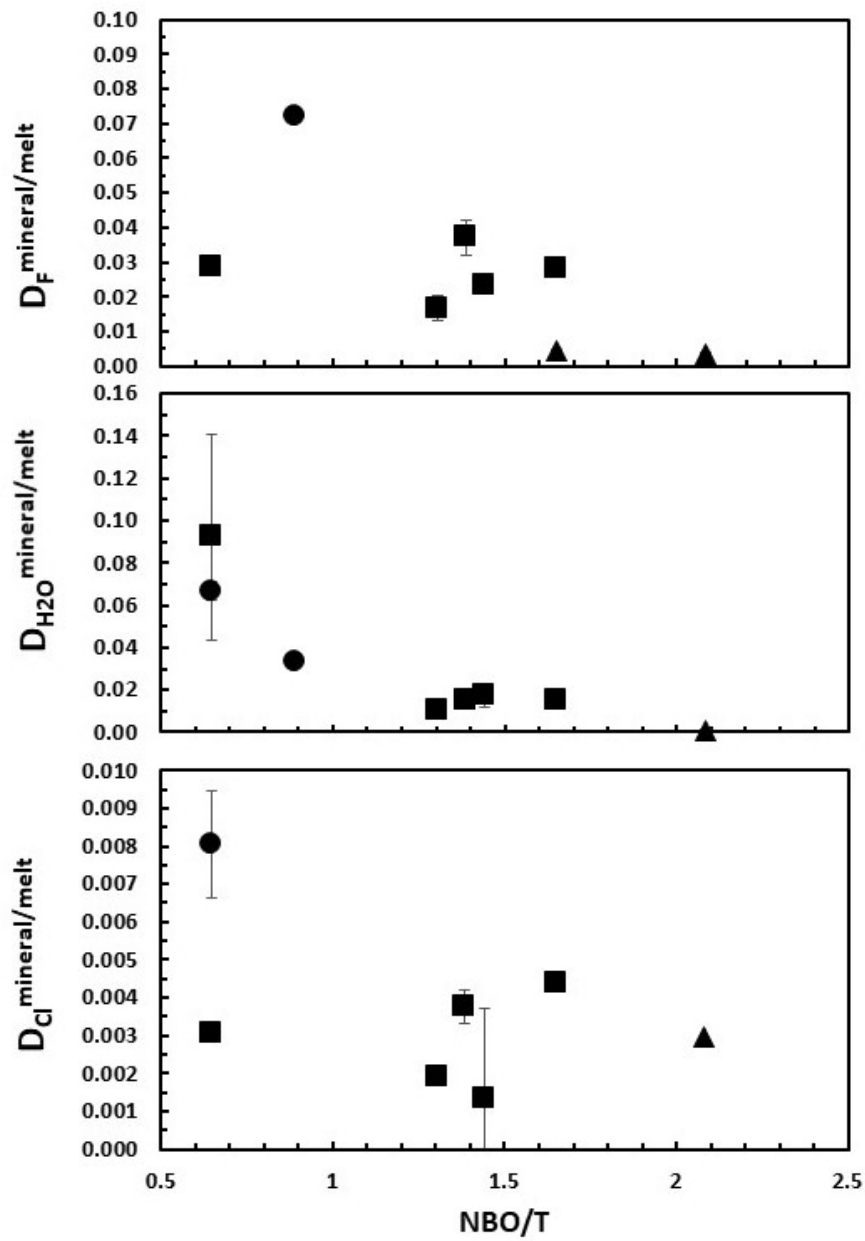
903

904

905   Figure 9: Results from modelling F, Cl and H_2O distribution during progressive solidification of a model LMO, using crystallisation sequence of
906   Rapp and Draper (2018) (grey boxes, from 0-97% solidification), based on CFHA* LMO model of McCubbin et al. (2015). A-B: solidification with
907   no inter-cumulate liquid. D-E: solidification with 1% intercumulate liquid. A and D show volatile content of liquid (magma) during progressive
908   solidification; F = black squares, H_2O = dark grey squares, Cl = light grey circles. B and E show volatile abundances in cumulate (same key). C
909   shows corresponding volatile ratios for cumulates with no intercumulate liquid (dashed lines) and 1% intercumulate liquid (solid lines): grey =
910   F/Cl, black = F/H2O. F shows volatile ratios in remaining liquid.
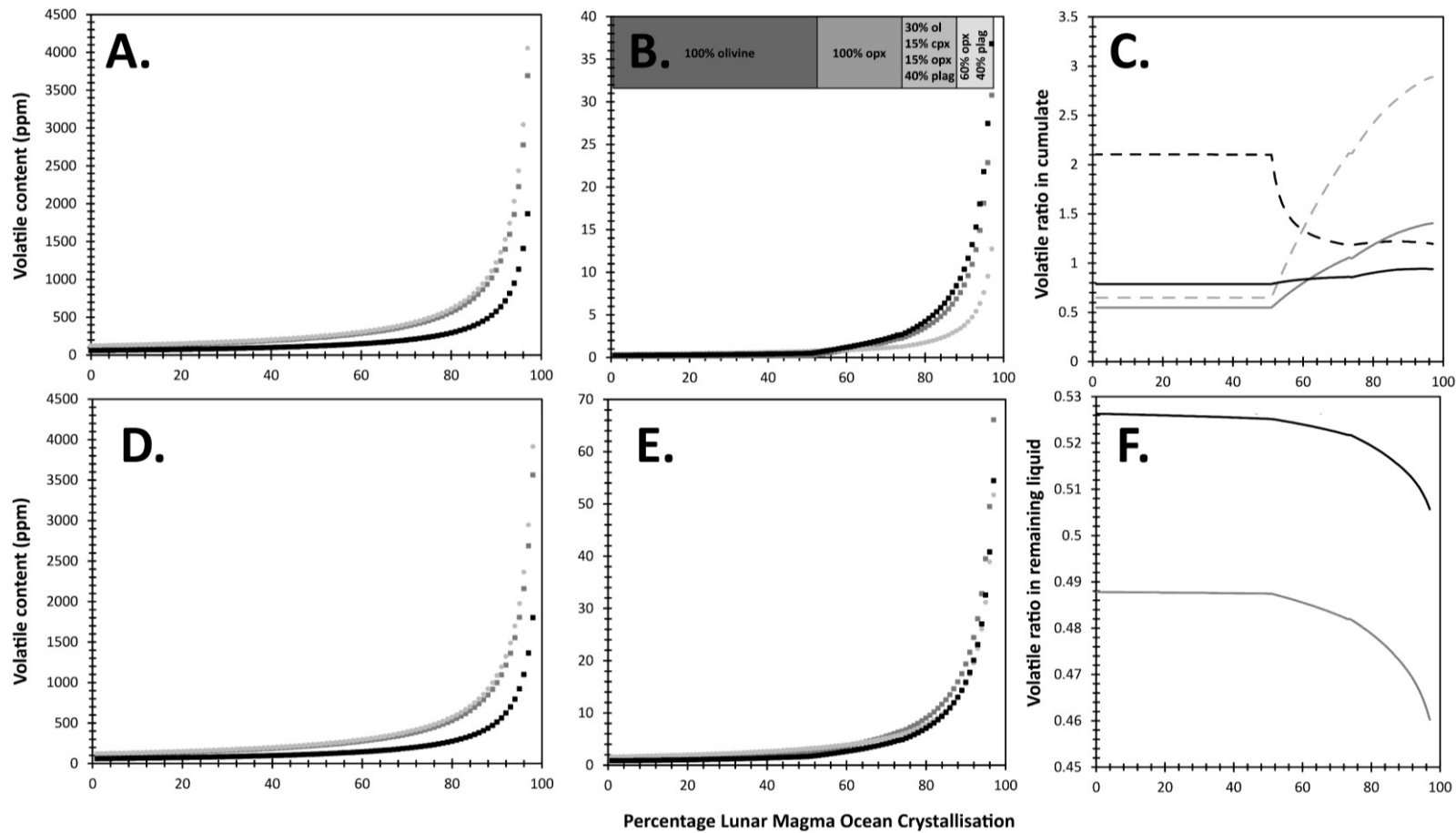
911

912   Albarède F. (2009) Volatile accretion history of the terrestrial planets and dynamic
913   implications. *Nature* **461**, 1227-1233.
914   Ardia P., Hirschmann M. M., Withers A. C. and Stanley B. D. (2013) Solubility of CH_4 in a
915   synthetic basaltic melt, with applications to atmosphere-magma ocean-core partitioning
916   of volatiles and to the evolution of the Martian atmosphere. *Geochim. Cosmochim. Acta*
917   **114**, 52–71.
918   Armstrong L. S., Hirschmann M. M., Stanley B. D., Falksen E. G. and Jacobsen S. D. (2015)
919   Speciation and solubility of reduced C-O-H-N volatiles in mafic melt: Implications for
920   volcanism, atmospheric evolution, and deep volatile cycles in the terrestrial planets.
921   *Geochim. Cosmochim. Acta* **171**, 283–302.
922   Barnes J. J., Franchi I. A., Anand M., Tartese R., Starkey N. A., Koike M., Sano Y. and
923   Russell S. S. (2013) Accurate and precise measurements of the D/H ratio and hydroxyl
924   content in lunar apatites using NanoSIMS. *Chem. Geol.* **337**, 48–55.
925   Barr, J.A. and Grove, T.L. (2013) Experimental petrology of the Apollo 15 group A green
926   glasses: Melting primordial lunar mantle and magma ocean cumulate assimilation.
927   Geochim. Cosmochim. Acta **106**, 216–230.
928   Barr J. A. and Grove T. L. (2007) Experimental petrology of Apollo 15 Group A ultramafic
929   green glasses: In search of a primordial lunar interior. In *Lunar and Planetary Science*
930   *XXXVIII*, Abstract #1194.
931   Beyer C., Klemme S., Wiedenbeck M., Stracke A. and Vollmer C. (2012) Fluorine in
932   nominally fluorine-free mantle minerals: Experimental partitioning of F between olivine,
933   orthopyroxene and silicate melts with implications for magmatic processes. *Earth*
934   *Planet. Sci. Lett.* **337**, 1–9.
935   Boyce J. W., Kanee S. A., McCubbin F. M., Barnes J. J., Bricker H. and Treiman A. H.
936   (2018) Early loss, fractionation, and redistribution of chlorine in the Moon as revealed
937   by the low-Ti lunar mare basalt suite. *Earth Planet. Sci. Lett.* **500**, 205–214.
938   Boyce J. W., Liu Y., Rossman G. R., Guan Y., Eiler J. M., Stolper E. M. and Taylor L. A.
939   (2010) Lunar apatite with terrestrial volatile abundances. *Nature* **466**, 466–469.
940   Boyce J.W, Treiman A.H., Guan Y.B., Ma C., Eiler J.M., Gross J., Greenwood J.P., Stolper
941   E.M. (2015) The chlorine isotope fingerprint of the lunar magma ocean. *Science*
942   *Advances* **1 (8)**, e1500380.
943   Bromiley G.D. and Hilairet N (2005) Hydrogen and minor element incorporation in synthetic
944   rutile. *Min. Mag.* **69** (3), 345-358.
945   Bromiley G. D. and Bromiley F. A. (2006) High-pressure phase transitions and hydrogen
946   incorporation in $MgSiO_3$ enstatite. *Am. Mineral.* **91**, 1094–1101.
947   Bromiley G. D., Brooke J. and Kohn S. C. (2017) Hydrogen and deuterium diffusion in non-
948   stoichiometric spinel. *High Press. Res.* **37**, 360–376.
949   Bromiley G. D., Keppler H., McCammon C., Bromiley F. A. and Jacobsen S. D. (2004a)
950   Hydrogen solubility and speciation in natural, gem-quality chromian diopside. *Am.*
951   *Mineral.* **89**.
952   Bromiley G.D., Hilaret N, and McCammon C. (2004b) Solubility of hydrogen and ferric iron in
953   rutile and TiO_2 (II): Implications for phase assemblages during ultrahigh-pressure
954   metamorphism and for the stability of silica polymorphs in the lower mantle. *Geophys.*
955   *Res. Lett.* **31**, L04610.
956   Brooker R., Holloway J.R. and Hervig R. L. (1998). Reduction in piston cylinder experiments:
957   The detection of carbon infiltration into platinum capsules. Amer. Mineral. **83**, 985-994.
958   Brown, S.M. and Grove, T.L. (2015) Origin of the Apollo 14, 15, and 17 yellow ultramafic
959   glasses by mixing of deep cumulate remelts. *Geochim. Cosmochim. Acta* **171**, 201–

960   215.

961   Canup B. and Agnor C. (2000) Accretion of the terrestrial planets and the Earth-Moon
962   system. In *Origin of the Earth and Moon* (eds. R. M. Canup and K. Righter). University
963   of Arizona Press. pp. 113–130.

964   Canup R. M. (2004) Dynamics of Lunar Formation. *Annu. Rev. Astron. Astrophys.* **42**, 411–
965   475.

966   Chen, H.K. and Lindsley, D.H. (1983). Apollo-14 Very Low Titanium glasses - melting
967   experiments in iron platinum alloy capsules. J. Geophys. Res. **88**, B335–B342.

968   Chen, H.K., Delano J. W., Lindsley, D.H. (1982) Chemistry and phase-relations of VLT
969   volcanic glasses from Apollo-14 and Apollo-17. J. Geophys. Res. **87(S)**, A171-A181

970   Chen Y., Zhang Y., Liu Y., Guan Y., Eiler J. and Stolper E. M. (2015) Water, fluorine, and
971   sulfur concentrations in the lunar mantle. *Earth Planet. Sci. Lett.* **427**, 37–46.

972   Cody G.D., Ackerson M., Beaumont C., Foustoukos D., Le Losq C., Mysen, B.O. (2020)
973   Revisiting water speciation in hydrous alumino-silicate glasses: A discrepancy between
974   solid-state ^{1}H NMR and NIR spectroscopy in the determination of X-OH and H_2O.
975   *Geochim. Cosmochim. Acta* **285**, 150-174.

976   Crepisson C., Blanchard M., Bureau H., Sanloup C., Withers A. C., Khodja H., Surble S.,
977   Raepsaet C., Beneut K., Leroy C., Giura P. and Balan E. (2014) Clumped fluoride-
978   hydroxyl defects in forsterite: Implications for the upper-mantle. *Earth Planet. Sci. Lett.*
979   **390**, 287–295.

980   Dalou C., Koga K. T., Shimizu N., Boulon J. and Devidal J.-L. (2012) Experimental
981   determination of F and Cl partitioning between lherzolite and basaltic melt. *Contrib. to*
982   *Mineral. Petrol.* **163**, 591–609.

983   Delano J. W. (1979) Apollo 15 green glass: chemistry and possible origin. In *Proceedings of*
984   *the 10th Lunar and Planetary Science Conference* pp. 275–300.

985   Dixon J. E., Stolper E. M. and Holloway J. R. (1995) An experimental study of water and
986   carbon dioxide solubilities in mid ocean ridge basaltic liquids .1. Calibration and
987   solubility models. *J. Petrol.* **36**, 1607–1631.

988   Elardo S.M., Shearer C.K., Vander Kaaden K.E., McCubbin F.M. and Bell, A.S. (2015)
989   Petrogenesis of primitive and evolved basalts in a cooling Moon: Experimental
990   constraints from the youngest known lunar magmas. *Earth Planet. Sci. Lett.* **422**, 126–
991   137.

992   Elkins-Tanton, L.T., Chatterjee, N., and Grove, T.L. (2003) Experimental and petrological
993   constraints on lunar differentiation from the Apollo 15 green picritic glasses. Meteorit.
994   Planet. Sci. 38, 515–527.

995   Elkins-Tanton L. T. and Grove T. L. (2011) Water (hydrogen) in the lunar mantle: Results
996   from petrology and magma ocean modeling. *Earth Planet. Sci. Lett.* **307**, 173–179.

997   Grant K.J., Brooker R.A., Kohn S.C., and Wood B.J. (2007). The effect of oxygen fugacity on
998   hydroxyl concentrations and speciation in olivine: Implications for water solubility in the
999   upper mantle. *Earth Plant. Sci. Letts.*, **261**, 217-229.

1000   Greenwood J.P., Itoh S., Sakamoto N., Warren P., Taylor L., Yurimoto H. (2011) Hydrogen
1001   isotope ratios in lunar rocks indicate delivery of cometary water to the Moon, Nature
1002   GeoSci. **4**, 79-82.

1003   Greenwood J. P. (2018) Hydrogen and D/H analysis of apatite by Elemental Analyzer-
1004   Chromium/High-Temperature Conversion-Isotope Ratio Mass Spectrometry (EA-
1005   Cr/HTC-IRMS). *Chem. Geol.* **500**, 175–181.

1006   Greenwood J.P., Abe K., McKeeby B. (2020) Cl-bearing fluorcalciobritholite in high-Ti
1007   basalts from Apollo 11 and 17: Implications for volatile histories of late-stage lunar

1008   magmas. *Am. Mineral.* **105**, 255–261.

1009   Hauri E. H., Gaetani G. A. and Green T. H. (2006) Partitioning of water during melting of the
1010   Earth's upper mantle at H2O-undersaturated conditions. *Earth Planet. Sci. Lett.* **248**,
1011   715–734.

1012   Hauri E. H., Saal A. E., Rutherford M. J. and Van Orman J. A. (2015) Water in the Moon's
1013   interior: Truth and consequences. *Earth Planet. Sci. Lett.* **409**, 252–264.

1014   Hauri E. H., Weinreich T., Saal A. E., Rutherford M. C. and Van Orman J. A. (2011) High
1015   Pre-Eruptive Water Contents Preserved in Lunar Melt Inclusions. *Science.* **333**, 213–
1016   215.

1017   Hirschmann M. M., Withers A. C., Ardia P. and Foley N. T. (2012) Solubility of molecular
1018   hydrogen in silicate melts and consequences for volatile evolution of terrestrial planets.
1019   *Earth Planet. Sci. Lett.* **345**, 38–48.

1020   Holzheid A. and Oneill H. S. (1995) The Cr-Cr_2O_3 oxygen buffer and the free-energy of
1021   formation of Cr_2O_3 from high-temperature electrochemical measurements. *Geochim.*
1022   *Cosmochim. Acta* **59**, 475–479.

1023   Hui H., Peslier A. H., Zhang Y. and Neal C. R. (2013) Water in lunar anorthosites and
1024   evidence for a wet early Moon. *Nat. Geosci.* **6**, 177–180.

1025   Hui H., Guan Y., Chen Y., Peslier A.H., Zhang Y., Liu Y., Flemming R.L., Rossman G.R.,
1026   Eiler J.M., Neal C.R., and Osinski G.R. (2017) A heterogeneous lunar interior for
1027   hydrogen isotopes as revealed by the lunar highlands samples. *Earth Planet. Sci. Lett.*
1028   **473**, 14-23.

1029   Ingrin J. and Skogby H. (2000) Hydrogen in nominally anhydrous upper-mantle minerals:
1030   concentration levels and implications. *Eur. J. Mineral.* **12**, 543–570.

1031   Joachim B., Pawley A., Lyon I. C., Marquardt (nee Hartmann) K., Henkel T., Clay P. L.,
1032   Ruzie L., Burgess R. and Ballentine C. J. (2015) Experimental partitioning of F and Cl
1033   between olivine, orthopyroxene and silicate melt at Earth's mantle conditions. *Chem.*
1034   *Geol.* **416**, 65–78.

1035   Joachim B., Stechern A., Ludwig T., Konzett J., Pawley A., Ruzie-Hamilton L., Clay P. L.,
1036   Burgess R. and Ballentine C. J. (2017) Effect of water on the fluorine and chlorine
1037   partitioning behavior between olivine and silicate melt. *Contrib. to Mineral. Petrol.* **172**.

1038   Jochum K. P., Nohl L., Herwig K., Lammel E., Stoll B. and Hofmann A. W. (2005) GeoReM:
1039   A new geochemical database for reference materials and isotopic standards. *Geostand.*
1040   *Geoanalytical Res.* **29**, 333–338.

1041   Kadik A. A., Litvin Y. A., Koltashev V. V, Kryukova E. B. and Plotnichenko V. G. (2006)
1042   Solubility of hydrogen and carbon in reduced magmas of the early Earth's mantle.
1043   *Geochemistry Int.* **44**, 33–47.

1044   Krawczynski M.J. and Grove T.L. (2012) Experimental investigation of the influence of
1045   oxygen fugacity on the source depths for high titanium lunar ultramafic magmas.
1046   *Geochim. Cosmochim. Acta* **79**, 1-19.

1047   Klemme S. and Stalder R. (2018) Halogens in the Earth's Mantle: What We Know and What
1048   We Don't. In *role of halogens in terrestrial and extraterrestrial geochemical processes:*
1049   *surface, crust, and mantle* (ed. Harlov, DE and Aranovich, L). Springer Geochemistry.
1050   Springer International Publishing AG, Gewerbestrasse 11, Cham, CH-6330,
1051   Switzerland. pp. 847–869.

1052   Leitzke F.P., Fonseca R.O.C., Göttlicher J., Steininger R., Jahn S., Prescher C., and Lagos
1053   M. (2018) Ti K-edge XANES study on the coordination number and oxidation state of
1054   Titanium in pyroxene, olivine, armalcolite, ilmenite, and silicate glass during mare basalt
1055   petrogenesis. *Geochim. Cosmochim. Acta* **173**, 103.

1056 Lemaire C., Koh, S.C., Brooker R.A. (2004). The effect of silica activity on the incorporation
1057   mechanism of water in synthetic forsterite: a polarised infrared spectroscopic study.
1058   Contrib. Mineral. Petrol. **147**, 48-57.

1059 Lin Y. H., Hui H., Li Y., Xu Y. and van Westrenen W. (2019) A lunar hygrometer based on
1060   plagioclase-melt partitioning of water. *Geochemical Perspect. Lett.* **10**, 14–19.

1061 Longhi J. (1992) Experimental petrology and petrogenesis of mare volcanics. *Geochim.*
1062   *Cosmochim. Acta* **56**, 2235–2251.

1063 Lucey P., Korotev R. L., Gillis J. J., Taylor L. A., Lawrence D., Campbell B. A., Elphic R.,
1064   Feldman B., LL H., Hunten D., Mendillo M., Noble S., Papike J. J., Reedy R. C.,
1065   Lawson S., Prettyman T., Gasnault O. and Maurice S. (2006) Understanding the Lunar
1066   Surface and Space-Moon Interactions. In *New Views of the Moon* (eds. B. L. Jolliff, M.
1067   A. Wieczorek, C. K. Shearer, and C. R. Neal). Mineralogical Society of America,
1068   Geochemical Society, Chantilly, Virginia. pp. 83–220.

1069 Matjuschkin V., Brooker R.A., Tattitch B.T., Blundy J., Stamper C.C. (2015) Control and
1070   monitoring of oxygen fugacity in piston cylinder experiments. *Contrib Mineral Petrol*
1071   **169**, 9.

1072 Matveev S., Portnyagin M., Ballhaus C., Brooker R. and Geiger C. (2005). FTIR spectrum of
1073   phenocryst olivine as an indicator of silica saturation in magmas. J. Petrol. **46**, 603-614.

1074 McCubbin F. M., Jolliff B. L., Nekvasil H., Carpenter P. K., Zeigler R. A., Steele A., Elardo S.
1075   M. and Lindsley D. H. (2011) Fluorine and chlorine abundances in lunar apatite:
1076   Implications for heterogeneous distributions of magmatic volatiles in the lunar interior.
1077   *Geochim. Cosmochim. Acta* **75**, 5073–5093.

1078 McCubbin Francis M, Steele A., Hauri E. H., Nekvasil H., Yamashita S. and Hemley R. J.
1079   (2010a) Nominally hydrous magmatism on the Moon. *Proc. Natl. Acad. Sci. U.S.A.* **107**,
1080   11223–11228.

1081 McCubbin F M, Steele A., Nekvasil H., Schnieders A., Rose T., Fries M., Carpenter P. K.
1082   and Jolliff B. L. (2010b) Detection of structurally bound hydroxyl in fluorapatite from
1083   Apollo Mare basalt 15058,128 using TOF-SIMS. *Am. Mineral.* **95**, 1141–1150.

1084 McCubbin F.M., Vander Kaaden K.E., Tartèse R., Klima R.L., Mortimer J., Baarnes J.,
1085   Shearer C.K., Treiman A.H., Lawrence D.J., Elardo S.M., Hurley D.M., Boyce J.W., and
1086   Anand M. (2015) Magmatic volatiles (H, C, N, F, S, Cl) in the lunar mantle, crust, and
1087   regolith: Abundances, distributions, processes, and reservoirs. *Am. Mineral.* **100**, 1668–
1088   1707.

1089 Mosenfelder J. L. and Rossman G. R. (2013a) Analysis of hydrogen and fluorine in
1090   pyroxenes: I. Orthopyroxene. *Am. Mineral.* **98**, 1026–1041.

1091 Mosenfelder J. L. and Rossman G. R. (2013b) Analysis of hydrogen and fluorine in
1092   pyroxenes: II. Clinopyroxene. *Am. Mineral.* **98**, 1042–1054.

1093 Mysen B.O., Kumamoto K., Cody G.D., Fogel M.L. (2011) Solubility and solution
1094   mechanisms of C–O–H volatiles in silicate melt with variable redox conditions and melt
1095   composition at upper mantle temperatures and pressures. *Geochim et Cosmochim*
1096   *Acta* **75**, 6183–6199.

1097 Newcombe M.E., Brett A., Beckett J.R., Baker M.B., Newman S., Guan Y., Eiler J.M.,
1098   Stolper E.M. (2017) Solubility of water in lunar basalt at low $p\mathrm{H_2O}$. *Geochim.*
1099   *Cosmochim. Acta* **200**, 330-352.

1100 Ni P., Zhang Y., Chen S. and Gagnon J. (2019) A melt inclusion study on volatile
1101   abundances in the lunar mantle. *Geochim. Cosmochim. Acta* **249**, 17–41.

1102 Ni P., Zhang Y. and Guan Y. (2017) Volatile loss during homogenization of lunar melt
1103   inclusions. *Earth Planet. Sci. Lett.* **478**, 214–224.

1104 O'Leary J.A., Gaetani G.A. and Hauri E.H. (2010) The effect of tetrahedral Al^{3+} on the
1105   partitining of water between clinopyroxene and silicate melt. *Earth Planet. Sci. Lett.*
1106   **297**, 111-120.
1107 Pandya N., Muenow D. W. and Sharma S. K. (1992) The effect of bulk composition on the
1108   speciation of water in submarine volcanic glasses. *Geochim. Cosmochim. Acta* **56**,
1109   1875–1883.
1110 Peslier A. H. (2010) A review of water contents of nominally anhydrous natural minerals in
1111   the mantles of Earth, Mars and the Moon. *J. Volcanol. Geotherm. Res.* **197**, 239–258.
1112 Potts N. J., Barnes J. J., Tartese R., Franchi I. A. and Anand M. (2018) Chlorine isotopic
1113   compositions of apatite in Apollo 14 rocks: Evidence for widespread vapor-phase
1114   metasomatism on the lunar nearside similar to 4 billion years ago. *Geochim.*
1115   *Cosmochim. Acta* **230**, 46–59.
1116 Rapp J. F. and Draper D. S. (2018) Fractional crystallization of the lunar magma ocean:
1117   Updating the dominant paradigm. *Meteorit. Planet. Sci.* **53**, 1432–1455.
1118 Rosenthal A., Hauri E. H. and Hirschmann M. M. (2015) Experimental determination of C, F,
1119   and H partitioning between mantle minerals and carbonated basalt, CO_2/Ba and
1120 CO_2/Nb systematics of partial melting, and the CO_2 contents of basaltic source regions.
1121   *Earth Planet. Sci. Lett.* **412**, 77–87.
1122 Rutherford M. J. and Papale P. (2009) Origin of basalt fire-fountain eruptions on Earth
1123   versus the Moon. *Geology* **37**, 219–222.
1124 Ryder G. (1991) Lunar ferroan anorthosites and mare basalt sources - the mixed connection.
1125   *Geophys. Res. Lett.* **18**, 2065–2068.
1126 Saal A. E., Hauri E. H., Van Orman J. A. and Rutherford M. J. (2013) Hydrogen Isotopes in
1127   Lunar Volcanic Glasses and Melt Inclusions Reveal a Carbonaceous Chondrite
1128   Heritage. *Science.* **340**, 1317–1320.
1129 Saal A., Hauri E., Lo Cascio M., Van Orman J. A., Rutherford M. C. and Cooper R. F. (2008)
1130   Volatile content of lunar volcanic glasses and the presence of water in the Moon's
1131   interior. *Nature* **454**, 192–196.
1132 Sato M. (1976) Oxygen fugacity and other thermochemical parameters of Apollo 17 high-Ti
1133   basalts and their impilcations on the reduction mechanism. In *Conference Proceedings*
1134   *of the 7th Lunar Science Conference* pp. 1323–1344.
1135 Shearer C. K., Hess P. C., Wieczorek M. A., Pritchard M. E., Parmentier E. M., Borg L. E.,
1136   Longhi J., Elkins Tanton L. T., Neal C. R., Antonenko I., Canup R. M., Halliday A. N.,
1137   Grove T. L., Hager B. H., Lee D.-C. and Wiechert U. (2006) Thermal and Magmatic
1138   Evolution of the Moon. In *Reviews in Mineralogy and Geochemistry* (eds. B. L. Jolliff, M.
1139   A. Wieczorek, C. K. Shearer, and C. R. Niel). Chantilly, Virginia. pp. 365–518.
1140 Shishkina T.A., Botcharnikov R.A., Holtz F., Almeev R.R. and Portnyagin M.V. (2010)
1141   Solubility of H_2O- and CO_2-bearing fluids in tholeiitic basalts at pressures up to 500
1142   MPa. *Chem. Geol.* **277** (1-2), 115-125.
1143 Skogby H., Bell D. R. and Rossman G. R. (1990) Hydroxide in pyroxene: variations in the
1144   natural environment. *Am. Mineral.* **75**, 764–774.
1145 Smyth J. R., Bell D. R. and Rossman G. R. (1991) Incorporation of hydroxyl in upper-mantle
1146   clinopyroxenes. *Nature* **351**, 732–735.
1147 Smyth J. R., Frost D. J., Nestola F., Holl C. M. and Bromiley G. D. (2006) Olivine hydration
1148   in the deep upper mantle: Effects of temperature and silica activity. *Geophys. Res. Lett.*
1149   **33**, L15301.
1150 Stalder R. (2004) Influence of Fe, Cr and Al on hydrogen incorporation in orthopyroxene.
1151   *Eur. J. Mineral.* **16**, 703–711.

1152 Stalder R. and Skogby H. (2003) Hydrogen diffusion in natural and synthetic orthopyroxene.
1153   *Phys. Chem. Miner.* **30**, 12–19.
1154 Stokes T. N. (2019). The crystal chemistry of accessory minerals as a probe of magmatic
1155   oxygen fugacity: an experimental study. PhD thesis, University of Edinburgh.
1156 Stokes T. N., Bromiley G. D., Potts N. J., Saunders K. E., Miles A. J. and EIMF (2019) The
1157   effect of melt composition and oxygen fugacity on manganese partitioning between
1158   apatite and silicate melt. *Chem. Geol.* **506**, 162–174.
1159 Stolper E. (1982) The speciation of water in silicate melts. *Geochim. Cosmochim. Acta* **46**,
1160   2609–2620.
1161 Taylor S. R., Pieters C. M. and MacPherson G. J. (2006) Earth-moon system, planetary
1162   science, and lessons learned. In *New views of the Moon* (ed. Jolliff, BL and Wieczorek,
1163   MA). Reviews in Mineralogy & Geochemistry. Mineralogical Soc Amer, 3635 Concorde
1164   Pkwy STE 500, Chantilly, VA 20151-1125 USA. pp. 657–704.
1165 Tenner T.J., Hirschmann M.M., Withers A.C., and Hervig, R.L. (2009) Hydrogen partitioning
1166   between nominally anhydrous upper mantle minerals and melt between 3 and 5 GPa
1167   and applications to hydrous peridotite partial melting. *Chem. Geol.* **262**, 42–56.
1168 Treiman A. H., Boyce J. W., Gross J., Guan Y., Eiler J. M. and Stolper E. M. (2014)
1169   Phosphate-halogen metasomatism of lunar granulite 79215: Impact-induced
1170   fractionation of volatiles and incompatible elements. *Am. Mineral.* **99**, 1860–1870.
1171 Urann B. M., Le Roux V., Hammond K., Marschall H. R., Lee C.-T. A. and Monteleone B. D.
1172   (2017) Fluorine and chlorine in mantle minerals and the halogen budget of the Earth's
1173   mantle. *Contrib. to Mineral. Petrol.* **172**.
1174 Wade J. and Wood B.J. (2005) Core formation and the oxidation state of the Earth. *Earth
1175   Planet. Sci. Lett.* **236**, 78–95.
1176 Yang X., Keppler H. and Li Y. (2016) Molecular hydrogen in mantle minerals. *Geochemical
1177   Perspect. Lett.* **2**, 160.
1178 Walker D., Longhi, J., Stolper, E.M., Grove T.L., Hays J.F. (1975) Origin of titaniferous lunar
1179   basalts. *Geochim. Cosmochim. Acta* **39**, 1219-1235.
1180 Warren, P.H. (1985) The magma ocean concept and lunar evolution. *Annu. Rev. Earth
1181   Planet. Sc.* **13**, 201–240.
1182 Zhang Li, Guo X., Li W.-C., Ding J., Zhou D., Zhang Lingmin and Ni H. (2019)
1183   Reassessment of pre-eruptive water content of lunar volcanic glass based on new data
1184   of water diffusivity. *Earth Planet. Sci. Lett.* **522**, 40–47.
1185
1186